



Downward continued multichannel seismic refraction analysis of Atlantis Massif oceanic core complex, 30°N, Mid-Atlantic Ridge

A. S. Henig, D. K. Blackman, and A. J. Harding

Scripps Institution of Oceanography, University of California, San Diego, 9500 Gilman Drive, La Jolla, California 92093-0225, USA (ahenig@ucsd.edu)

J.-P. Canales

Department of Geology and Geophysics, Woods Hole Oceanographic Institution, MS 24, 360 Woods Hole Road, Woods Hole, Massachusetts 02543-1050, USA

G. M. Kent

Nevada Seismological Lab, University of Nevada, MS-174, Reno, Nevada 89557, USA

[1] Detailed seismic refraction results show striking lateral and vertical variability of velocity structure within the Atlantis Massif oceanic core complex (OCC), contrasting notably with its conjugate ridge flank. Multichannel seismic (MCS) data are downward continued using the Synthetic On Bottom Experiment (SOBE) method, providing unprecedented detail in tomographic models of the P-wave velocity structure to seafloor depths of up to 1.5 km. Velocities can vary up to 3 km/s over several hundred meters and unusually high velocities (~5 km/s) are found immediately beneath the seafloor in key regions. Correlation with *in situ* and dredged rock samples, video and records from submersible dives, and a 1.415 km drill core, allow us to infer dominant lithologies. A high velocity body(ies) found to shoal near to the seafloor in multiple locations is interpreted as gabbro and is displaced along isochrons within the OCC, indicating a propagating magmatic source as the origin for this pluton(s). The western two-thirds of the Southern Ridge is capped in serpentinite that may extend nearly to the base of our ray coverage. The distribution of inferred serpentinite indicates that the gabbroic pluton(s) was emplaced into a dominantly peridotitic host rock. Presumably the mantle host rock was later altered via seawater penetration along the detachment zone, which controlled development of the OCC. The asymmetric distribution of seismic velocities and morphology of Atlantis Massif are consistent with a detachment fault with a component of dip to the southeast. The lowest velocities observed atop the eastern Central Dome and conjugate crust are most likely volcanics. Here, an updated model of the magmatic and extensional faulting processes at Atlantis Massif is deduced from the seismic results, contributing more generally to understanding the processes controlling the formation of heterogeneous lithosphere at slow-rate spreading centers.

Components: 15,700 words, 11 figures, 1 table.

Keywords: Mid-Atlantic Ridge; detachment fault; gabbro; oceanic core complex; seismic structure; serpentinitized peridotite.

Index Terms: 3025 Marine Geology and Geophysics: Marine seismics (0935, 7294); 3035 Marine Geology and Geophysics: Midocean ridge processes; 3045 Marine Geology and Geophysics: Seafloor morphology, geology, and geophysics.

Received 20 January 2012; **Revised** 19 April 2012; **Accepted** 20 April 2012; **Published** 19 May 2012.

Henig, A. S., D. K. Blackman, A. J. Harding, J.-P. Canales, and G. M. Kent (2012), Downward continued multichannel seismic refraction analysis of Atlantis Massif oceanic core complex, 30°N, Mid-Atlantic Ridge, *Geochem. Geophys. Geosyst.*, 13, Q0AG07, doi:10.1029/2012GC004059.

Theme: Oceanic Detachment Faults

1. Introduction

[2] Lithospheric heterogeneity is the result of ridge processes that vary in time and space, and to first order, structural differences in slow-spread lithosphere produce anomalous seafloor morphology [e.g., Cannat *et al.*, 2006] interrupting the more common abyssal hill pattern. Early studies of gravity structure at the Mid-Atlantic Ridge (MAR) suggest crustal thickness variations of several kilometers along the ridge axis over length scales of several hundred kilometers [Kuo and Forsyth, 1988; Lin *et al.*, 1990; Morris and Detrick, 1991; Michael *et al.*, 1994; Detrick *et al.*, 1995] and across transform faults, while across-axis, smaller-scale gravity studies suggest crustal thickness differences can also occur on conjugate sides of the ridge [Blackman *et al.*, 1998, 2008].

[3] Regional seismic investigations also indicate a heterogeneous slow-spread lithospheric structure at the segment scale. Seismic imaging of the crust along the axis of various spreading segments shows several kilometers of thinning between segment center and segment end that is dominantly controlled by thickness variations in the lower crustal layer [e.g., Tolstoy *et al.*, 1993; Hooft *et al.*, 2000; Planert *et al.*, 2009]. These crustal thickness variations are often accompanied by lateral changes in seismic velocity [e.g., Canales *et al.*, 2000a; Hooft *et al.*, 2000]. Seismically determined changes in thickness and structure of igneous crust are also documented across axis [Canales *et al.*, 2000b]. Denser local seismic studies show dramatic changes in seismic structure at lateral scales of a few kilometers [Canales *et al.*, 2008; Xu *et al.*, 2009; Arnulf *et al.*, 2011].

[4] Geologic studies also show that the classic homogeneous layered model of oceanic crust [Penrose Conference Participants, 1973], where erupted basalts overlie sheeted dikes and gabbro at depth, is only one of many crustal structures possible. Outcrops of serpentinized peridotite and gabbro [Cannat, 1993; Dick *et al.*, 2008], in contrast to the expected erupted basalt, have been identified at the seafloor on ridge flanks of slow spreading centers by submersible [Karson, 1999;

Blackman *et al.*, 2002; Boschi *et al.*, 2006; Tucholke and Lin, 1994] and drilling studies [Dick *et al.*, 2000; MacLeod *et al.*, 2002; Kelemen *et al.*, 2004; Blackman *et al.*, 2006]. All of these observations illustrate the spatially and temporally irregular magmatic processes and faulting styles that typify slow-spreading ridges and control the formation of heterogeneous crust and lithosphere.

[5] Oceanic core complexes (OCCs), lower crustal and mantle sections exhumed by detachment faulting, are formed at slow and intermediate spreading centers [Cann *et al.*, 1997; Tucholke *et al.*, 1998, 2001; Ohara *et al.*, 2001; Reston *et al.*, 2002; Searle *et al.*, 2003; Smith *et al.*, 2006, 2008], probably in association with long lived detachment faulting that persists for up to over 1 Myr [Tucholke *et al.*, 1998; Grimes *et al.*, 2008]. The OCCs are domal and characterized by their high relief, often kilometers above surrounding seafloor, and by the presence of spreading-parallel corrugations on the capping surface that have 10's m amplitude and km-scale wavelengths [Cann *et al.*, 1997; Tucholke *et al.*, 1998]. The corrugations document sustained relative motion between the exposed footwall and previously overlying hanging wall. Recent studies show that detachment faulting is a prominent process along portions of all slow spreading oceanic ridges [Cannat *et al.*, 2006; Smith *et al.*, 2006; Escartin *et al.*, 2008] and is likely controlled by temporally changing magmatic conditions [Ildefonse *et al.*, 2007; Tucholke *et al.*, 2008; MacLeod *et al.*, 2009; Olive *et al.*, 2010]. Numerical models estimate that during lithospheric creation, the formation of detachment faults near the ridge occurs when magmatic accretion is active between 30–50% of the time, while the remainder of plate separation is due to tectonic extension [Buck *et al.*, 2005; Tucholke *et al.*, 2008; Olive *et al.*, 2010]. At these rates of magmatism, plutons can be emplaced in the ultramafic host-rock forming a plum-pudding style lithosphere [Cannat, 1993; Escartin *et al.*, 2003; Ildefonse *et al.*, 2007] and can be denuded to the seafloor due to motion on one of these detachment faults. Determination of the internal structure of OCCs can provide insight into the magmatic conditions during their formation and perhaps constrain the extent of alteration.

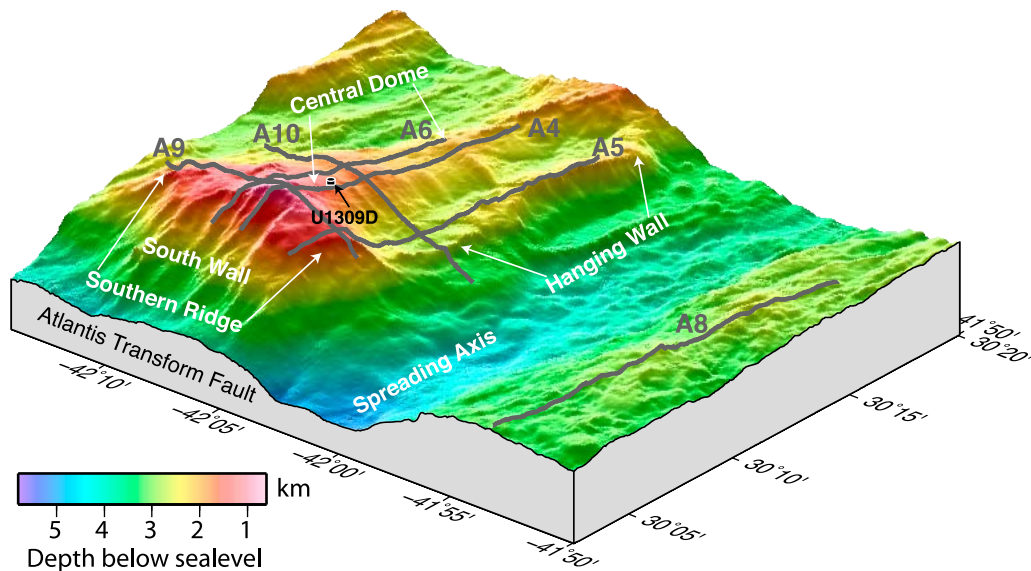


Figure 1. Perspective view of the Atlantis Massif looking to the northwest. Labels indicate the three main morphologic components and the South Wall. The Mid-Atlantic Ridge Axis and Atlantis Transform Fault are indicated. Gray lines and labels show location and extent of coverage for the six MultiChannel Seismic lines in this study. The location of IODP Hole U1309D is shown by the black cylinder.

[6] In this paper, we present a detailed seismic refraction study of the Atlantis Massif OCC (Figure 1), a young and well-mapped OCC on the Mid-Atlantic Ridge, and its conjugate crust, with the main objective of characterizing structural variability and magmatic history in this location. Three OCCs occur along the Atlantis transform fault (ATF) within lithosphere formed in the last 10 Myr [Canales *et al.*, 1997], suggesting continued episodicity in magma supply. Seismic imaging of the OCC allows us to constrain vertical and lateral variations in seismic velocity and we can employ these velocity structure observations in a lithologic and evolutionary analysis of Atlantis Massif.

[7] Our study expands on the multichannel seismic (MCS) refraction study of Canales *et al.* [2008], where only two MCS lines were analyzed with sea surface data, to include the full dataset covering the massif. We use an innovative downward continuation technique [Harding *et al.*, 2007; Arnulf *et al.*, 2011] to process the seismic data. The downward continuation technique has not previously been applied to a study of an OCC, therefore this study provides insights into how this method performs in high relief areas with high subsurface velocities and velocity gradients [Canales *et al.*, 2008].

[8] We present tomographic models for 5 seismic lines covering the dome of the massif, which show heterogeneity of seismic structure and a decent correlation with in situ rock samples from seafloor

outcrops. In addition, the model for one seismic line along the conjugate crust at the other side of the MAR axis serves to highlight the anomalous character of the OCC. Based on our tomographic results, we develop a model for how faulting and magmatism evolved to produce the observed structure at Atlantis Massif.

2. Methods

2.1. Data Acquisition

[9] Five intersecting MCS lines covering the dome of the Atlantis Massif and one line on the conjugate crust across the spreading axis from the OCC were collected aboard the R/V Maurice Ewing during the cruise EW-0102 in 2001 [Canales *et al.*, 2004]. The seismic lines range in length from ~21 to ~27 km and comprise between 85 and 109 shots each in this study. Water depth varies greatly, from 785 m to nearly 3.25 km on the OCC, and the conjugate crust line is over seafloor depths of 2.5–3.15 km. The greatest relief on a single line is 1.67 km.

[10] The survey source consisted of a 10-airgun array with total capacity of 3100 in³ (51 l) towed at 8 m depth and fired approximately every 37.7 m. Receivers spaced 12.5 m along a 6 km long, 480-channel streamer recorded the returning energy at a depth of approximately 10 m. *In situ* source and receiver positions were determined from shipboard

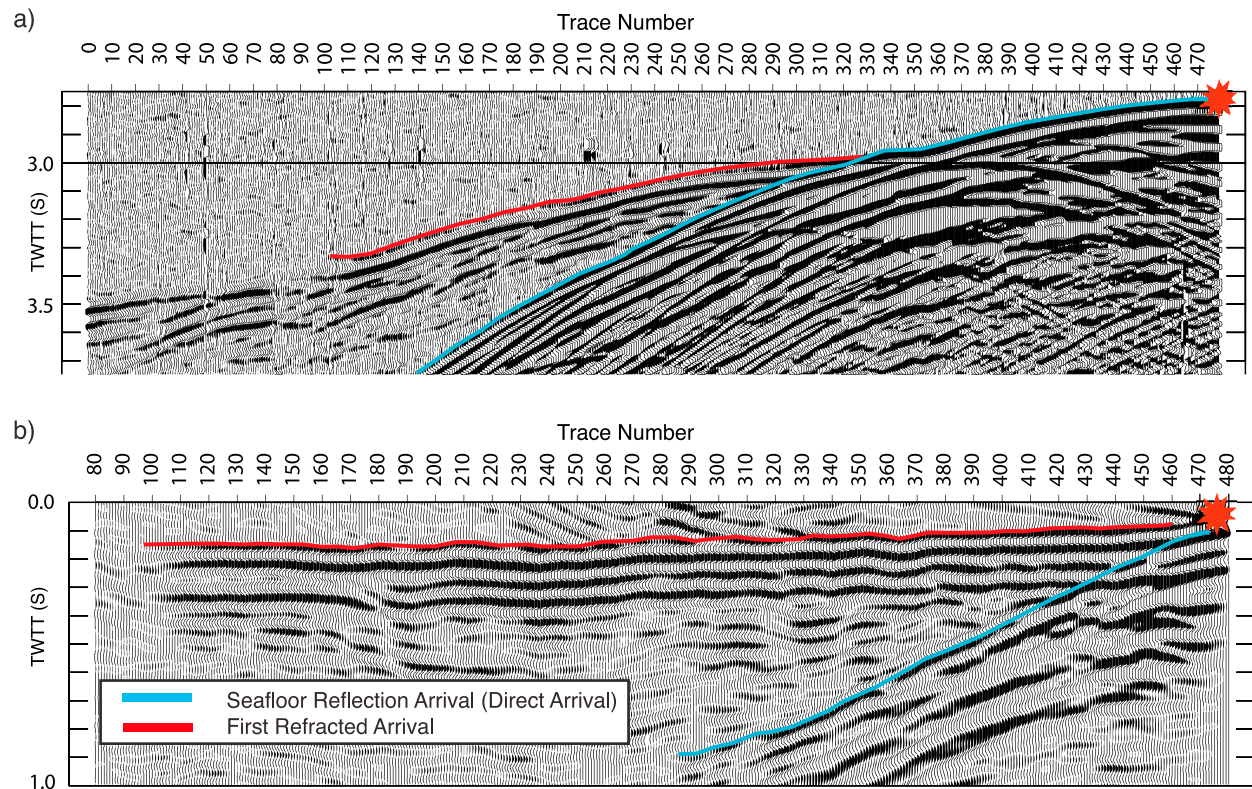


Figure 2. Representative shot gathers illustrating the result of the Synthetic On-Bottom Experiment downward continuation technique and plotted with a reduction velocity of 6.5 km/s. (a) Initial shot gather before SOBE processing. (b) SOBE processed shot gather showing collapse of seafloor reflection arrival and exposure of near-offset first refracted arrivals. Cyan marks seafloor reflection arrival; red marks first refracted arrival. Red stars indicate the end of the streamer closest to the source.

GPS, tail-buoy GPS recordings and compass-enhanced DigiCourse birds attached to the streamer [Canales *et al.*, 2008].

[11] Seismic velocity models from lines A4 and A10 were previously published by Canales *et al.* [2008] using standard processing techniques. This study extends analysis to all six seismic lines surveying the OCC and the conjugate crust, including the previously studied lines A4 and A10, and makes use of a downward continuation processing method. Of the five OCC lines, two are parallel to the spreading direction (A9 and A10) and three are subparallel to the strike of the spreading axis (A4, A6, and A5), while the conjugate crust line A8 is subparallel to the MAR axis (Figure 1).

2.2. SOBE Downward Continuation and Additional Data Processing

[12] We employ a method in which shots and receivers are downward continued to the seafloor using a Kirchhoff phase shift redatuming algorithm [Shtivelman and Canning, 1988]. This process creates a Synthetic On-Bottom Experiment (SOBE)

[Harding *et al.*, 2007; Arnulf *et al.*, 2011] that exposes the shallowest turning basement refractions as first arrivals by collapsing the water wave (the first seafloor reflection arrival) toward a point at zero-offset, and mostly unwrapping triplications produced by high gradient zones (Figure 2).

[13] The SOBE technique is most useful in areas of large water depth and low subsurface velocities. In such survey conditions, the majority of the streamer channels record the seafloor reflection arriving ahead of the crustal refraction arrival, making it difficult to obtain useful travel-time picks for rays traveling through the shallow crust. In shallow water, or where the ratio of basement to water velocities is high, only the nearest offset streamer channels will record the reflection ahead of the refraction. In this case travel times of crustal refractions can be picked directly without use of downward continuation. In water depths of ~ 3 km however, refracted data from at least the first 2 km of receivers are preceded by reflections.

[14] This redatuming allows shallow, refracted energy that would generally be obscured by the seafloor

reflection in deep water depths to be emergent (i.e., first arrivals), corresponding to raypaths in the upper few hundred meters of the subseafloor section. Travel-time picks of these near-offset crustal refractions thus provide excellent structural detail in the upper portion of our models. By improving the velocity detail in the upper region of the models, we also obtain better resolution of the deeper (400–1500 m) structure. Streamer tomography exploits the dense and even spatial distribution of MCS data, and is further improved upon by SOBE, which allows for the inclusion of shallower refractions that were only previously obtainable using either seafloor receivers and/or sources.

[15] The first refracted arrival is clearly observed in SOBE shot gathers for most of this data set and the signal-to-noise ratio (SNR) is generally high. Besides downward continuation or redatuming, minimal processing of the data was required. Prior to downward continuation, trace balancing was applied and consistently noisy traces were replaced by interpolation from the adjacent traces as continuity of seismic data across all streamer channels is required for downward continuation. The data were then downward continued in shot gather space, with a 5–20 Hz bandpass filter to exclude noise and unusable frequencies in the refraction data, followed by downward continuation in common receiver location space with a 20 Hz lowpass filter to minimize spatial aliasing. A fourth-order Butterworth filter was used in both steps and a water velocity of 1.5 km/s was assumed for the downward continuation.

2.3. Picking of Travel-Times

[16] Travel times of first arrival P-wave refractions were picked for every fifth shot gather along each MCS line. This corresponds to picking at a spacing of approximately 188.5 meters, which falls within the first Fresnel zone of ~ 200 m at the seafloor. In areas where a fifth gather was of poor quality, two nearby gathers were substituted in that interval to maintain at least one sampling in each Fresnel Zone. Travel times from all receivers were picked if each recorded a clear and continuous arrival (Figures 2b and 3a). Despite SOBE processing, in some cases it was not possible to pick the arrival all the way in to nearest offset, and this near offset data may have been missing from the original surface recording. In some areas of rough topography and low subsurface velocities, the water wave does not collapse down to a single point, but continues to have some finite width that obstructs the first

refracted arrival in a handful of the nearest offset traces (Figure 3).

[17] Data quality is generally good for most shot-receiver pairs, with the exception of a few locations where the SNR is lower due to a variety of possible factors. Complicated subsurface structure (Figure 3b), side-swipe from nearby seafloor structure (Figure 3c), and rough seafloor topography (Figure 3d) may all lower the SNR. Although minimized where possible, migration artifacts from noise and amplitude variability can also interfere with actual arrivals reducing the clarity of the arrival. No picks were made for receivers with intersecting noise or at breaks in the refracted arrivals. Where possible, traces with low SNR were picked by comparison with traces of the same offset in nearby shots.

[18] Pick uncertainties for lines A4, A6, A9, and A10 were generally between 10–30 ms, with 40 ms being the highest uncertainty assigned (Table 1). Line A5 pick uncertainties were assigned larger values, between 24–80 ms, due to a lower signal-to-noise ratio caused by the rough topography associated with the hanging wall along this line (Figure 1). Travel times for the first refracted arrival were picked both by hand and cross-correlation. When the cross-correlation technique was employed, the generated picks were visually inspected and adjusted by hand if necessary. Pick coverage for the five OCC lines covering the massif is shown in Figure 4. The coverage is evenly distributed along lines and the near-offsets are well sampled.

2.4. Tomographic Inversion

[19] We follow the method of *Van Avendonk et al. [2004]* to perform tomographic inversions of first crustal refraction travel times of the SOBE data. Our goal is to obtain the smoothest models that fit the data within the pick uncertainties with the fewest number of iterations. To measure the success of this travel-time fitting, the weighted misfit functional value χ^2 is used:

$$\chi^2 = \frac{1}{N} \sum_{i=1}^N \frac{(T_{obs,i} - T_{pred,i})^2}{\sigma_{unc,i}^2} \quad (1)$$

where T_{obs} is a picked travel-time, T_{pred} is a predicted travel-time of the ray through the current model, σ_{unc} is a pick uncertainty, and N is the total number of picks. Models are updated by minimizing the misfit between the predicted times and the

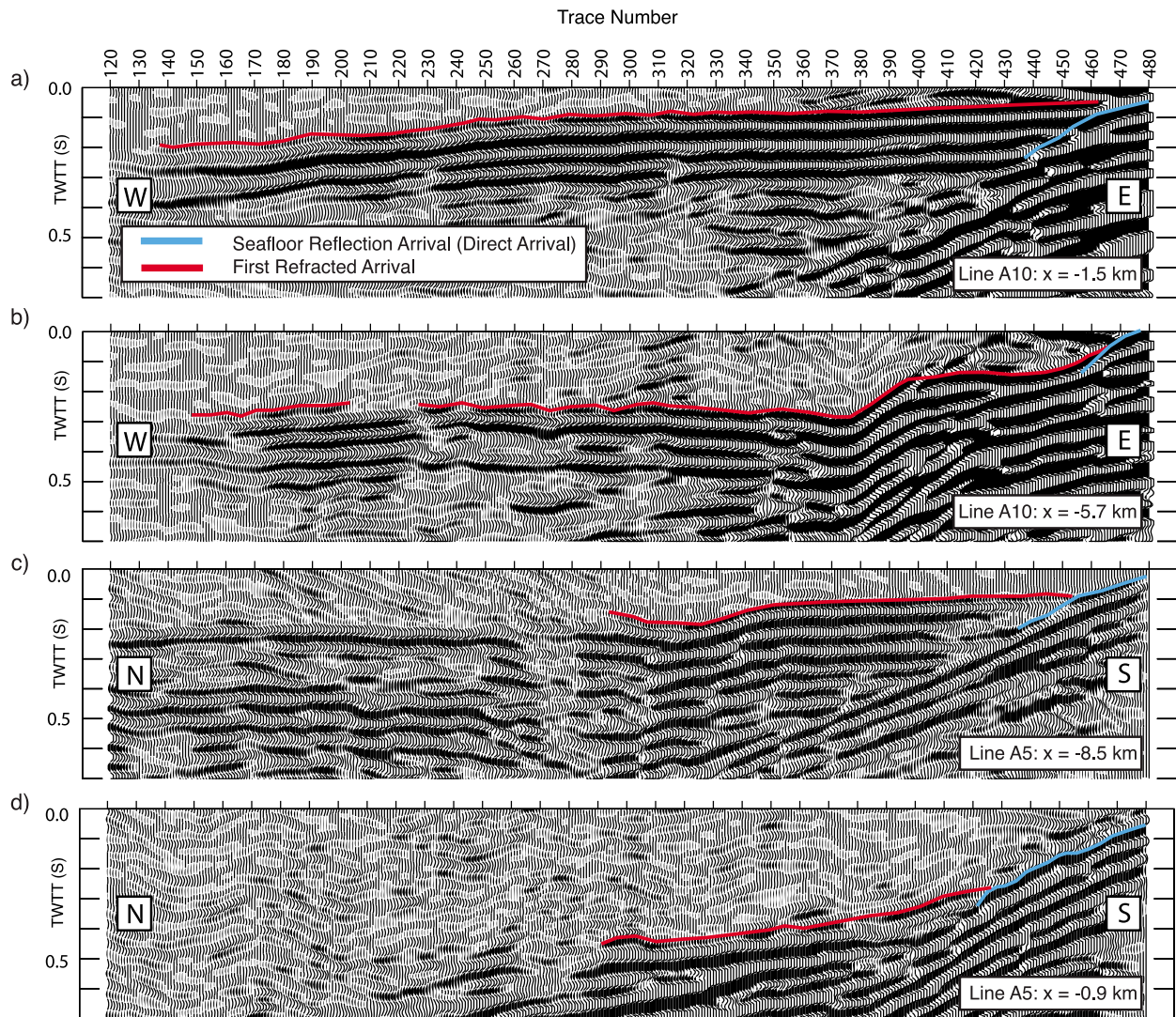


Figure 3. Representative shot gathers from the Atlantis Massif dataset showing a range of data quality. Trace number 480 is closest to the source. All shot gathers have been downward continued using SOBE. Shot gather locations are (a) atop the Central Dome, (b) on the Central Dome in an area of rapidly changing seismic structure, (c) the transition from hanging wall to Southern Ridge where out of plane echoes may be causing destructive interference at long ranges, and (d) atop the volcanic hanging wall in very rough topography. N, S, E, W indicate directions.

picked times in a least squares sense. Iterations are performed to fit the data until smoothing constraints are satisfied and an overall misfit $\chi^2 \approx 1$ is achieved (Table 1), indicating the desired fit of the observed

travel-times to within their uncertainties. Attention is paid to overall travel-time fit (represented by the χ^2 value), as well as to the distribution of misfit in individual shot gathers and regions (Figure 4).

Table 1. Select Inversion Parameters and Results for Preferred Models

Line	χ^2	$TTResids_{initial}$ Mean, [abs(max)]	$TTResids_{final}$ Mean, [abs(max)]	Uncert, σ	Horiz:Vert Aspect Ratio
A4	1.07	35.4, [189.6] ms	-1.9, [77.0] ms	10–20 ms	2
A5	0.94	-25.7, [440.2] ms	-3.9, [92.6] ms	24–80 ms	3
A6	1.03	10.4, [166.2] ms	-2.9, [83.5] ms	15–30 ms	2
A9	1.12	-45.1, [256.1] ms	-0.3, [106.8] ms	12–40 ms	2
A10	0.89	-4, [230.6] ms	-2.9, [82.5] ms	15–30 ms	2

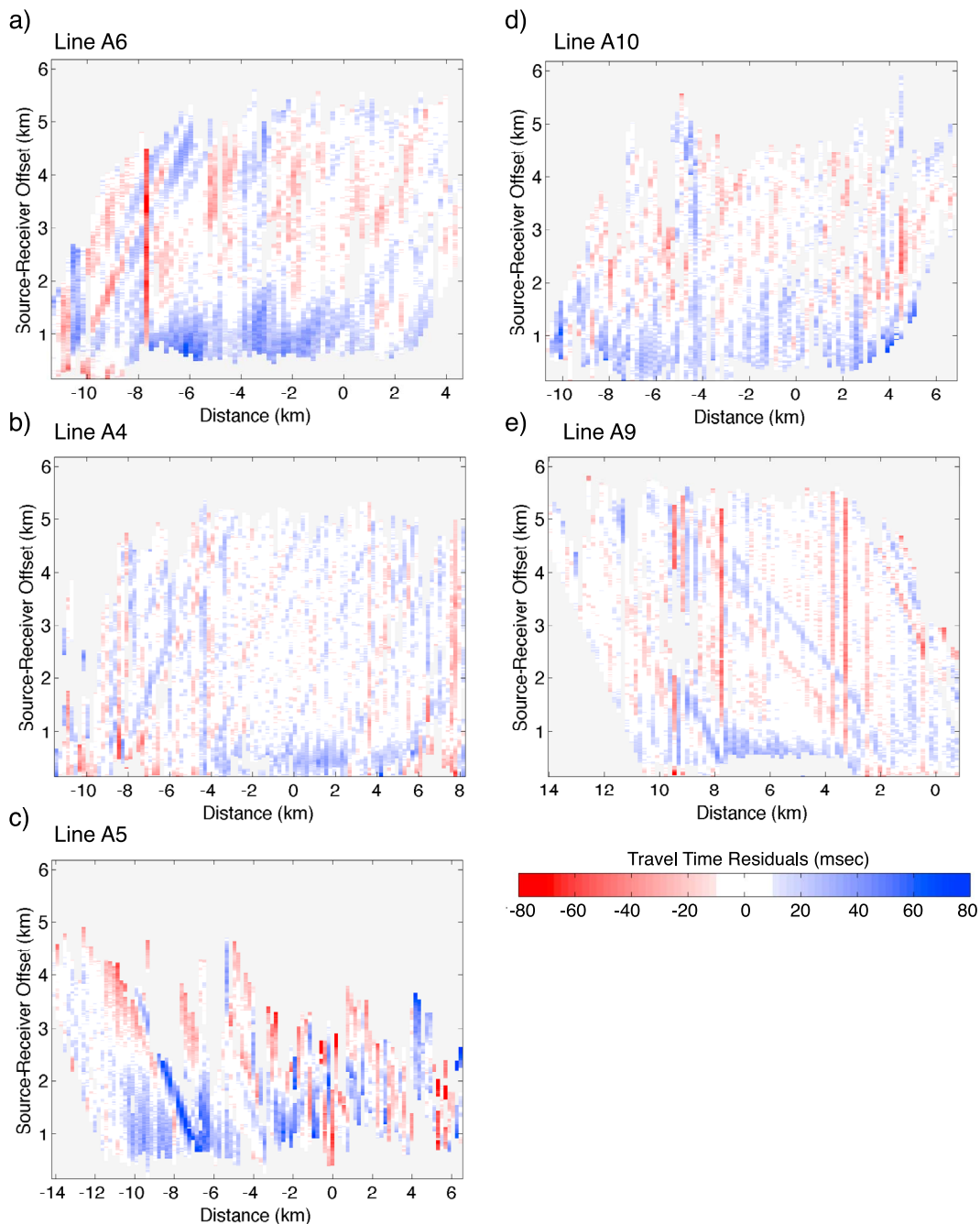


Figure 4. Travel time residuals with respect to the preferred model (Figure 6) as a function of model distance and source-receiver range.

[20] The tomographic inversions of each line proceeded through a series of linearized 2D inversions, followed by model update, and ray tracing in the new model. At each inversion step, the target misfit reduction was chosen small enough to satisfy the linearity assumption and the smoothing trade-off parameter was adjusted by the program to hit the target misfit [Van Avendonk *et al.*, 2004]. The models converged to their final misfits of 0.89–1.12

in 7 to 11 iterations (Table 1). The parameter controlling the relative strength of horizontal to vertical smoothing, a value chosen subjectively based on *a priori* expectations of the structure, is reduced as the inversion progresses to promote more rapid convergence of the model. Varying these parameters in this way allows the inversion first to fit large scale structure required by the data, and then to fine-tune smaller scale features. A low value of 2 or 3

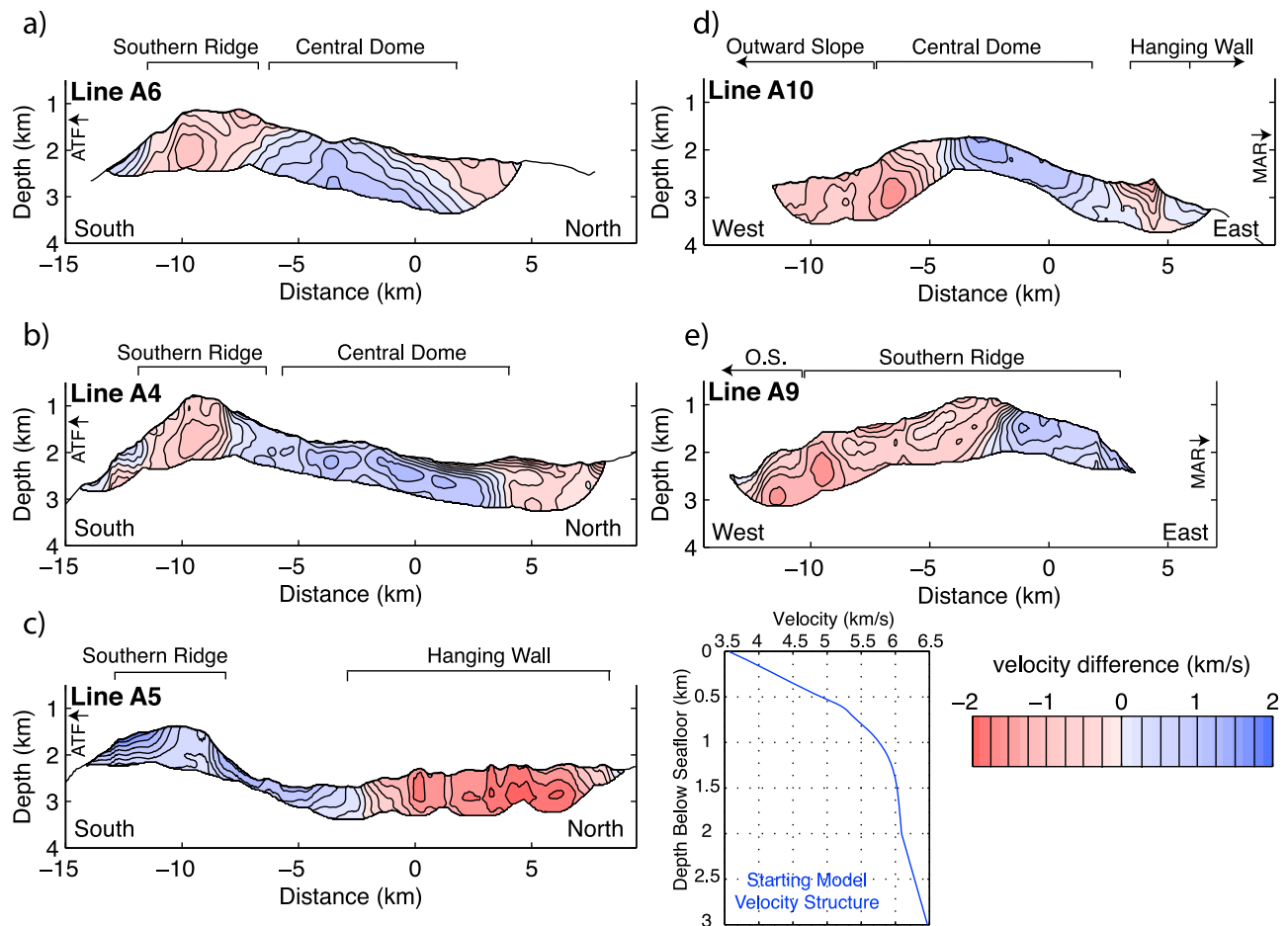


Figure 5. Difference between preferred and starting velocity models. Inset shows 1D starting model for all OCC lines. Contours are every 0.25 km/s.

(Table 1), depending on the model, for the final ratio of horizontal to vertical smoothing required to fit the data, indicates strongly laterally heterogeneous structure. The sequence of reductions in the aspect ratio parameters differs for each inversion for our preferred 2D models. This enables optimal fits for each line and allows different scales of structure to be resolved for each profile depending on what is required by the data. The grid spacing used in all inversions is 50 m in the x-direction and 25 m in the z-direction.

[21] For all the inversions, the starting model was a 1-D velocity profile, previously used in early downward continued tomographic analysis of line A10 [Harding *et al.*, 2007], hung from the seafloor (1D profile shown as inset in Figure 5). High residual travel times of the picks traced through the starting model indicate that the initial model deviates significantly from the actual velocity structure at Atlantis Massif (Table 1).

[22] Figure 4 shows the travel-time residuals of the picked data with respect to the preferred models for each MCS line. The residuals are significantly lower in the preferred models than in the starting models indicating a marked improvement in structural fidelity of the preferred models (Table 1). The residuals are typically <50 ms (maximum of <100 ms) throughout the profiles indicating that all parts of the model are fit about equally well by the data.

[23] Misfit problems arise in some areas of rough topography (scattering) due to difficulty in travel-time picking, in the vicinity of drastic slope changes, and where the bathymetry profile used in the inversion differs slightly from the actual bathymetry due to inadequate sonar centerbeam resolution. Mismatch of bathymetry results in high residuals that create diagonal streaks in shot-receiver space (Figure 4c) along a series of adjacent shots. Occasionally single or a few traces will have weak

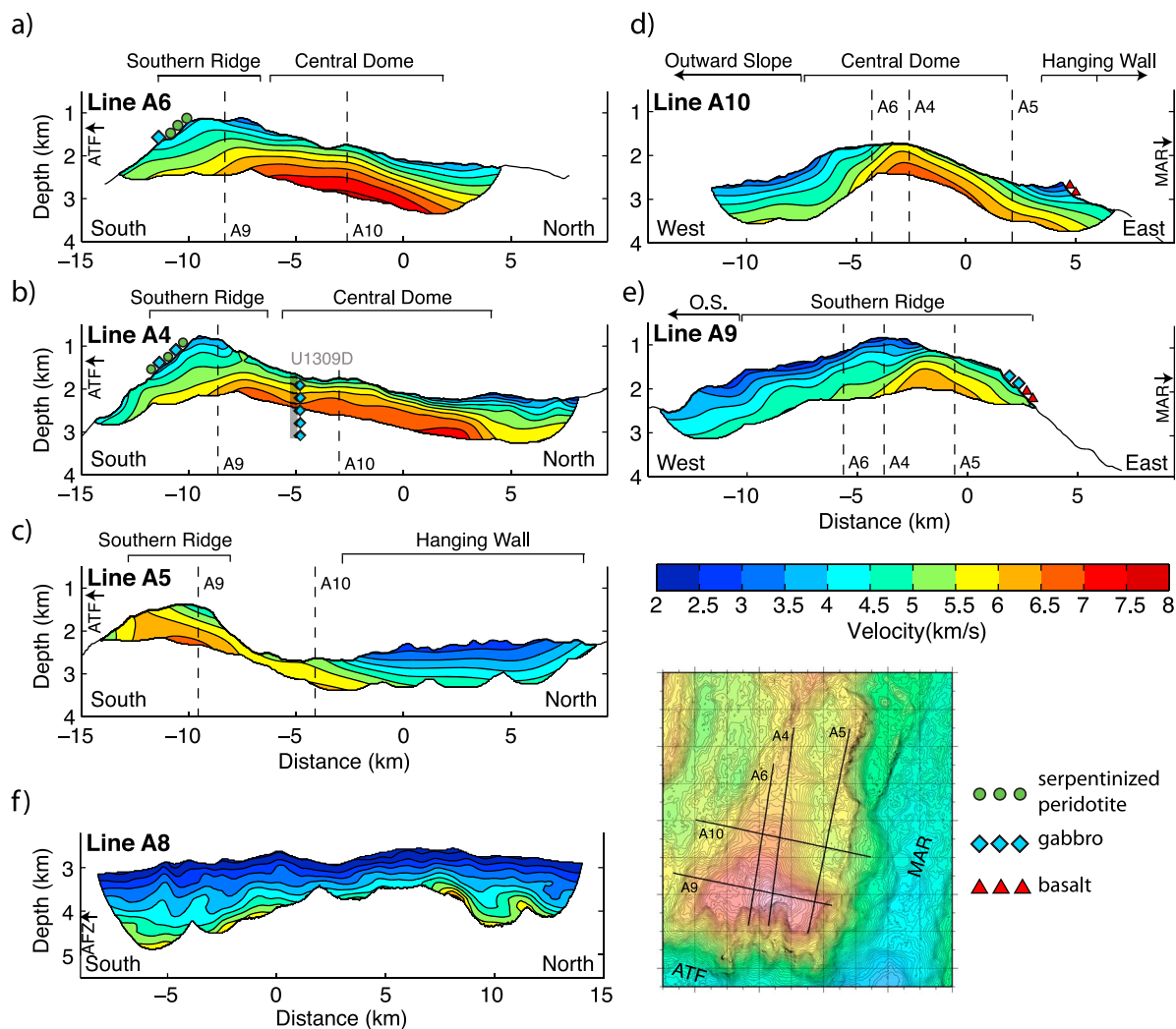


Figure 6. 2-D tomography models of P-wave velocity within (a–e) Atlantis Massif and (f) its conjugate crust depicted with 2:1 vertical exaggeration. (left) Ridge-parallel lines and (right) spreading-parallel lines. Line locations are shown in map view (inset) and major morphologic components are labeled at the top of each panel. Vertical dashed lines show locations of line crossings. Contour interval is 0.5 km/s. Green circles (Serpentinite), blue diamonds (Gabbro), and red triangles (Basalt) show the location of various rock types sampled from the massif surface or basement outcrops in submersible studies and drilling of IODP hole U1309D (vertical gray line projected onto line A4).

amplitude of the first arrival, probably due to out-of-plane side-echo caused by local 3D structure creating destructive interference or to rough, steep topography. These traces cannot be picked. In areas of very high velocity gradients just beneath the seafloor, as in the central portion of line A6 (Figure 6a), the inversion has some difficulty in resolving the very low velocity top layer (~100 m thick) above higher velocity material. This causes the nearest offset residuals for that region (Figure 4a) to remain high despite the use of decreased vertical smoothing and starting models with low velocity top layers.

2.5. Line A8

[24] Modeling of Line A8 was slightly different from what has been described above. The data were processed to a datum using the SOBE technique as for the other lines, but traveltime picking and inversion were done following the procedures described in *Canales et al.* [2008]. Traveltime picking was done by combining manual picking with a semi-automated first-break picking routine. The tomographic inversion was conducted using a regularized non-linear inversion with spatial smoothing constraints on the roughness of the model [Zelt and Barton, 1998]. This inversion method employs

models with continuous velocities. Unlike the OCC line inversion technique [Van Avendonk *et al.*, 2004], it thus does not allow for an explicit velocity discontinuity at the seafloor. This flexibility is useful for the OCC profiles where basement velocities and gradients are higher and water depths are shallow enough that the shallowest turning energy is recorded within the streamer aperture.

3. Tomography Results

[25] Our preferred tomographic models for P-wave velocity structure of the five MCS lines covering Atlantis Massif are shown in Figures 6a–6e. On scales of less than a kilometer, the models exhibit an extreme degree of lateral heterogeneity when compared with the compilation of young Atlantic crustal velocity values published by White *et al.* [1992]. Plots of deviations of the tomographic models with respect to the initial one-dimensional starting model for the OCC lines are particularly useful for identifying lateral variations in velocity structure across the Atlantis Massif (Figure 5). In our models, crustal velocity values vary between 2–7.5 km/s, with few locations exceeding 7 km/s. Because of the shallow high velocities, high velocity gradients, and the fixed 6 km streamer length, refraction ray coverage in this experiment is limited approximately to the upper 1.5 km of structure.

[26] While we do notice patterns in absolute velocities, our results do not show a well-defined classification scheme for velocity gradients, in contrast to what Canales *et al.* [2008] and Xu *et al.* [2009] describe for several Atlantic OCCs. These two prior studies note that as absolute velocities at the seafloor increase, velocity gradients increase as well: where seafloor velocities are <3.4 km/s, gradients are <1 s⁻¹; areas with velocities between 3.4–4.2 km/s have gradients ranging from 1–3 s⁻¹; and where velocities are >4.2 km/s, gradients are >3 s⁻¹ [Canales *et al.*, 2008; Xu *et al.*, 2009]. In our results, velocity gradients range from ~1–6 s⁻¹ in the upper 500 mbsf where gradients vary the most, mainly independent of absolute velocity (Figure 7a). By 750 m below seafloor, nearly all velocities (except Line A5 in the region of extrusive volcanic material) reach values ranging from 4–6.5 km/s, well into velocities corresponding to intrusive, rather than extrusive, rock. We attribute the lack of correlation between gradients and absolute velocities to the improved vertical resolution of the SOBE tomography models, which confines high gradients to the shallowest parts of the structure.

[27] We choose to divide vertical velocity profiles into three groups, similar in velocity but not gradient, to the aforementioned groupings of Canales *et al.* [2008] and Xu *et al.* [2009], to aid in interpretation of rock type from seismic velocity. These groupings are as follows: a group with slow surface velocities between 2–3 km/s and base-of-coverage velocities of 4–4.5 km/s; an intermediate velocity group with surface velocities between 3–4.5 km/s and base-of-coverage velocities of 4.75–5.5 km/s; and a group with the highest velocities, >4.5 km/s at the seafloor trending to 5.5–7 km/s at the base of coverage. Figure 7b shows velocity-depth profiles taken from various locations throughout the models to illustrate the three velocity groupings we have defined. The locations of the velocity-depth profiles are noted and were chosen because they represent the clearest examples of the distinct velocity structures associated with discrete portions of the massif.

[28] To highlight deviations from the accepted norm, it is useful to compare our models to the seismic velocity structure (and later to the lithologic structure) of the classical, homogeneously layered, model of oceanic crustal structure. This “Penrose” model, based on ophiolite structure, consists of upper crust, divided into extrusive pillow basalts (layer 2A) atop sheeted dikes (layer 2B), overlying gabbro (layer 3), which in turn overlies the uppermost mantle [Penrose Conference Participants, 1973].

[29] One difficulty we face when interpreting the different velocity groupings of Atlantis Massif is to characterize the structure of ‘normal’ oceanic crust at slow spreading ridges. This difficulty arises in part because of the heterogeneity of crustal structure and in part because of the difficulty in obtaining reliable results, particularly for the shallowest crust. One, often used, means of characterizing the range of normal crust is to use compilations of previous velocity models such as White *et al.* [1992]. Unfortunately, the results in this compilation are almost certainly too high to represent the velocity of extrusive volcanics. The seafloor velocities in the White *et al.* [1992] compilation range upwards from 2.7 km/s (Figure 7c), while measurements of seafloor velocity at fast and intermediate spreading rate ridges are typically in the range 2.0–3.0 km/s [e.g., Harding *et al.*, 1993; Christeson *et al.*, 1994; Canales *et al.*, 2005]. The latter range spans the detailed results for the MAR from Hussenoeder *et al.* [2002] for 35°N on the MAR and Seher *et al.* [2010] for the Lucky Strike segment. We use results from line A8 on the conjugate crust across the ridge and the hanging wall section of line A5, together with a more extensive

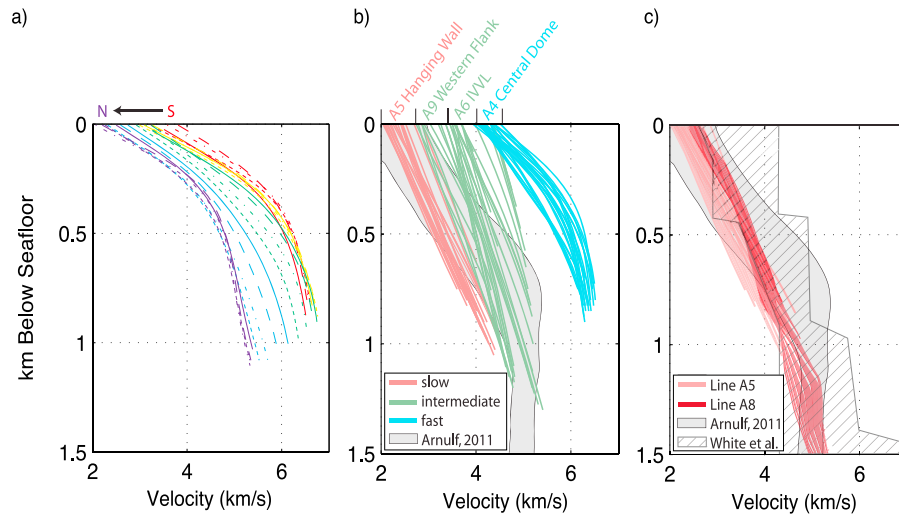


Figure 7. Velocity-depth profiles illustrating trends in velocities and velocity gradients within the models. (a) 1D profiles from the central dome along line A4 ($x = 1\text{--}6$ km) show that the highest velocity gradients occur within the upper ~ 400 m. Velocity-depth profiles are shown every 250 m along line portion. (b) Velocity-depth profiles showing the three velocity groupings determined from the models. Profiles come from various portions of the different lines and represent a sample every 250 m within the specified along-line range. The group of lowest seismic velocities (pink) range from 2–3 km/s to 4–4.5 km/s and were sampled between $x = 2\text{--}7$ km on line A5 (hanging wall); the group of intermediate velocities range from 3–4.5 km/s to 4.75–5.5 km/s (green) and were sampled from $x = -10$ to -5 km on line A9 (western flank of massif) and from $x = -13$ to -9 km on line A6; and the group of highest velocities (blue) range from >4.5 km/s to 5.5–7 km/s at the top and base of the ray coverage, respectively, and were sampled between $x = -4$ to 1 km on line A4 (Central Dome). No clear pattern in velocity gradients can be distinguished among the groups. (c) Comparison of velocity-depth profiles from line A5 hanging wall and line A8 on the low velocity, likely volcanic, conjugate crust with the velocity envelopes of the axial region of the Lucky Strike segment of the MAR (grey solid [Arnulf *et al.*, 2011; Arnulf, 2011]) and young Atlantic crust aged 0–7 Ma (hatched [White *et al.*, 1992]).

analysis of the Lucky Strike velocity range for 3-D tomography [Arnulf *et al.*, 2011; Arnulf, 2011] as the representation of non-OCC young Atlantic crustal values used for comparison with the Atlantis Massif results (Figure 7c).

3.1. Strike-Parallel Lines (Lines A6, A4, A5)

[30] The westernmost and central ridge-parallel lines (A6 and A4, respectively; Figures 6a and 6b) show a similar overall velocity pattern consisting of high velocities near the surface in the center of the lines grading into lower velocities on the south and north ends. Line A6, in older crust, however, exhibits a thicker section of lower velocities over the central part of the line when compared with line A4. The portion of line A6 between -3.5 km and -0.5 km in model space is also the location of highest velocity, with values >7.5 km/s at the base of the coverage (~ 1500 mbsf). The Southern Ridge velocities of 3–5 km/s contrast with the Central Dome velocities of 3.5–6.5 km/s as pointed out by Canales *et al.* [2008].

[31] Line A5, the easternmost ridge-parallel line crossing the remnant piece of hanging wall block,

shows very low velocities similar to those obtained for young, volcanic Atlantic crust using the SOBE method at the Lucky Strike segment of the MAR (Figure 7c) [Arnulf *et al.*, 2011]. These low velocities grade laterally very rapidly into high velocities in the 5–6 km/s range where the profile images the eastern flank of the Southern Ridge (Figure 6c). Neither here nor on line A10 do our inversions image a distinct velocity feature that might correspond to a detachment fault zone beneath the hanging wall. This could reflect a lack of distinct velocity structure or it could reflect the limited resolution of our models (~ 100 m) compared to the expected thickness of the detachment zone ($\sim 15\text{--}100$ m), based on structural and metamorphic geology studies at Atlantis Massif [e.g., Schroeder and John, 2004; Karson *et al.*, 2006; Blackman *et al.*, 2011; McCaig *et al.*, 2010].

3.2. Strike-Perpendicular Lines (Lines A9, A10)

[32] The two spreading-parallel lines, A10 and A9 (Figures 6d and 6e, respectively), are the most

heterogeneous in terms of velocity structure. Line A9, sampling the Southern Ridge, has velocities as high as 5 km/s directly at the seafloor on the eastern flank. The top portion of the massif in the central and western Southern Ridge and its western flank are significantly different than its eastern flank. A transition takes place across a few hundred meters lateral distance from high surface velocities in the east down to low values between 2.5–3 km/s in the center and western portions (Figure 6e). In the central and western Southern Ridge, velocity structure is similar to, but slightly faster than, young Atlantic crust (Figure 7b) [Arnulf *et al.*, 2011].

[33] For line A10 crossing the Central Dome, the highest subseafloor velocities (>5.5 km/s) are near the shallowest part of the Central Dome, several kilometers to the west of the high velocity peak of line A9. To the west in profile A10, as in A9, velocity values rapidly transition to significantly reduced crustal values over a few hundred horizontal meters (Figure 6d). These lowest velocities are found on the westernmost part of the line nearest the breakaway. On the eastern flank, line A10 samples the low velocity hanging wall underlain within 500 meters subseafloor by velocities >5 km/s.

3.3. Conjugate Ridge Flank Line A8

[34] Line A8 (Figure 6f) runs along crust that was accreted at the time of formation of the OCC but was transferred to the conjugate flank, therefore it was part of the hanging wall to the detachment fault. Seafloor morphology along the line is characteristic of volcanic terrain [e.g., *Smith and Cann*, 1993], suggesting that this profile represents primarily structure corresponding to extrusive volcanics. This profile shows overall less heterogeneity than the rest of the models, and its average velocity is the lowest of all (Figures 6 and 7c). It shows similar structure to the northern section of A5 over the hanging wall, with shallow most velocities of 2 km/s increasing to 5 km/s at 1.5 km bsf.

3.4. Model Resolution

[35] Very dense ray coverage exists in the portions of the models presented (down to ~1.5 km; Figure 6) with the exception of small slivers <100 m wide at the trailing end of the lines. The models are truncated (in white) in areas where rays only provide nominal influence on the structure. Thus we can resolve nearly all structure greater than a couple hundred meters in size.

[36] In areas where residuals are non-zero indicating an imperfect fit to the data (Figure 4), uncertainty of the models is modest. On line A6 for example, the nearest offset residuals are consistently about 50 ms (Figure 4a); we attribute this to a possible thin low velocity layer that is difficult for the inversion to resolve. In order to reconcile this 50 ms discrepancy, the topmost layer of line A6 (~150 m and 3.5 km/s in preferred model) would need to be ~170 m thicker or ~0.5 km/s slower.

4. Discussion

4.1. SOBE

[37] This study provides the first application of the SOBE technique in a shallow, high-relief topographic area with subsurface structure consisting of very high velocities and gradients. The SOBE technique provides improvement over regular shot gathers in areas of shallow, smooth topography and high subsurface velocities. In these areas, such as over the eastern Southern Ridge and atop the Central Dome, SOBE gathers show clear, robust, and coherent arrivals that are easily tracked and picked (Figures 2b and 3a). During the downward continuation process, few processing artifacts obscure the data in these settings.

[38] In areas of rougher topography, SOBE produces data of high enough quality to obtain a reasonable model, which may not be the case for standard surface data. In these rough areas, such as the hanging wall of line A5, refractions are weaker and arrivals are shorter than in areas of smooth topography and high velocities (Figure 3), but nonetheless SOBE provides an improvement over standard shot gathers in these areas.

[39] As evidenced by the residuals for line A5, great improvement in the fit of the model occurs over the high velocity, shallow Southern Ridge portion of the profile (Figure 4c, $x = -14$ to -9 km). Over the rough topography and very low velocity portion of this line (Figure 3c, $x = -4$ to 6 km), there is a broader range of residual values that have no coherent distribution. Roughness of topography causing side scatter together with slight misfit between centerbeam bathymetry and seismically determined seafloor may also contribute to this problem.

4.2. Lithology/Velocity Correlation

[40] Lithologic interpretations of our seismic results are guided by groundtruth data. As seismic velocities are non-unique and individual outcrops may

be smaller than the dimensions we can resolve, we aim to interpret general, dominant lithologies only. Some rock types have characteristic velocity ranges that may overlap, so we use available independent constraints to distinguish between lithologies. With the exception of the drill site on the Central Dome, all samples from Atlantis Massif are from within ~ 500 m of the pre-mass wasting surface of the OCC [Schroeder and John, 2004]; headwall scarps at the top of the South Wall allow seafloor access beyond the typical few meters. In Figure 6, we project onto each profile the results of rock sampling within ~ 2 km of a given profile so seismic structure can be readily compared with surface samples.

4.2.1. Relatively High Velocity Body (HVB)

[41] At Atlantis Massif, our models show high seismic velocities, 5 km/s or greater, outcropping essentially at the seafloor or within a couple hundred meters of the seafloor in several regions. Such high values at shallow depths are atypical for young Atlantic crust based on previous seismic studies [White *et al.*, 1992; Hussenoeder *et al.*, 2002; Arnulf *et al.*, 2011; Arnulf, 2011], although with the recent recognition of the prevalence of detachment faulting and core complexes at slow spreading centers [Smith *et al.*, 2006, 2008; Escartín *et al.*, 2008] these high velocities may occur more commonly than previously understood. The high velocities are also clearly distinct from the structure on the conjugate flank, which indicates that lithospheric accretion during OCC formation is highly asymmetric. Our seismic results thus support the extensive evidence previously documenting asymmetric lithospheric accretion [e.g., Kuo and Forsyth, 1988; Allerton *et al.*, 2000; Okino *et al.*, 2004].

[42] When addressing the lithologic ambiguity of seismic velocities in this case, we rule out the likelihood that these high velocities represent weakly fractured peridotite or minimally altered serpentinite because we expect degrees of alteration in both cases to exceed those that would produce *in situ* velocities significantly larger than 5 km/s (see subsequent discussion). Estimates for the amount and degree of serpentinization indicate moderate to major alteration of peridotite has occurred [Blackman *et al.*, 2002; Früh-Green *et al.*, 2003], making minimally serpentinized, or fractured yet unaltered, peridotite unlikely.

[43] Instead, this zone of velocities is characterized by the following features previously associated with gabbro [White *et al.*, 1992]: velocities >5.5 km/s close to the seafloor, and a relatively low velocity

gradient. IODP Hole U1309D, which is situated within this high velocity zone, retrieved predominantly gabbro down to a depth of 1.415 km [Blackman *et al.*, 2006, 2011]. The borehole sonic log velocities from U1309D [Collins *et al.*, 2009] are in good agreement with the vertical velocity profile taken from the nearest shot on the line nearest to the location of the drill site (Figure 8a). Canales *et al.* [2008] also interpret similar seismic velocity structure at the Kane and Dante's Domes OCCs as gabbro based on seafloor samples from Kane and drilling results from Atlantis Bank OCC on the Southwest Indian Ridge [Dick *et al.*, 2000]. We therefore associate the highest velocities in our models, the high velocity body (HVB), with rock of predominantly gabbroic composition.

[44] Lines A10 and A9 show that the high velocity body(ies) of the Central Dome occurs ~ 3.5 km to the west of the velocity high in the Southern Ridge (Figures 6d and 6e). Figure 8b shows the approximate extent of the HVB, projected onto the seafloor, based on our models. The peaks of the high velocity material are offset between the Central Dome and Southern Ridge in such a way that high velocity material in the south would have been emplaced ~ 0.15 – 0.3 Myr later than high velocity material in the Central Dome, assuming that the OCC-bearing ridge flank accommodated 50–100% of the uniform full spreading rate of 24 km/Myr [Sempère *et al.*, 1995; Zervas *et al.*, 1995]. Although there is no age dating from the Southern Ridge gabbroic core, age dating performed on material from the IODP drill hole suggests that construction of the Central Dome gabbroic core took place in two magmatic events spanning a period of as much as 0.15 Myr [Grimes *et al.*, 2008]. Therefore, it is possible that the gabbroic core in the Southern Ridge was constructed ~ 3.5 km to the east as part of the second (and perhaps even subsequent) construction event(s).

[45] From our seismic results alone however, we cannot definitively distinguish between a high velocity regime that is continuous or made up of discrete few-km scale bodies. In a subsequent section we describe possible scenarios for interplay between detachment faulting and intrusive magmatism that could produce the imaged structure.

4.2.2. Intermediate-Valued Velocity Layer (IVVL)

[46] In contrast to the high velocity areas peaking near the surface of the massif, there are also sections of the models composed of comparatively lower velocity material that are nevertheless distinct

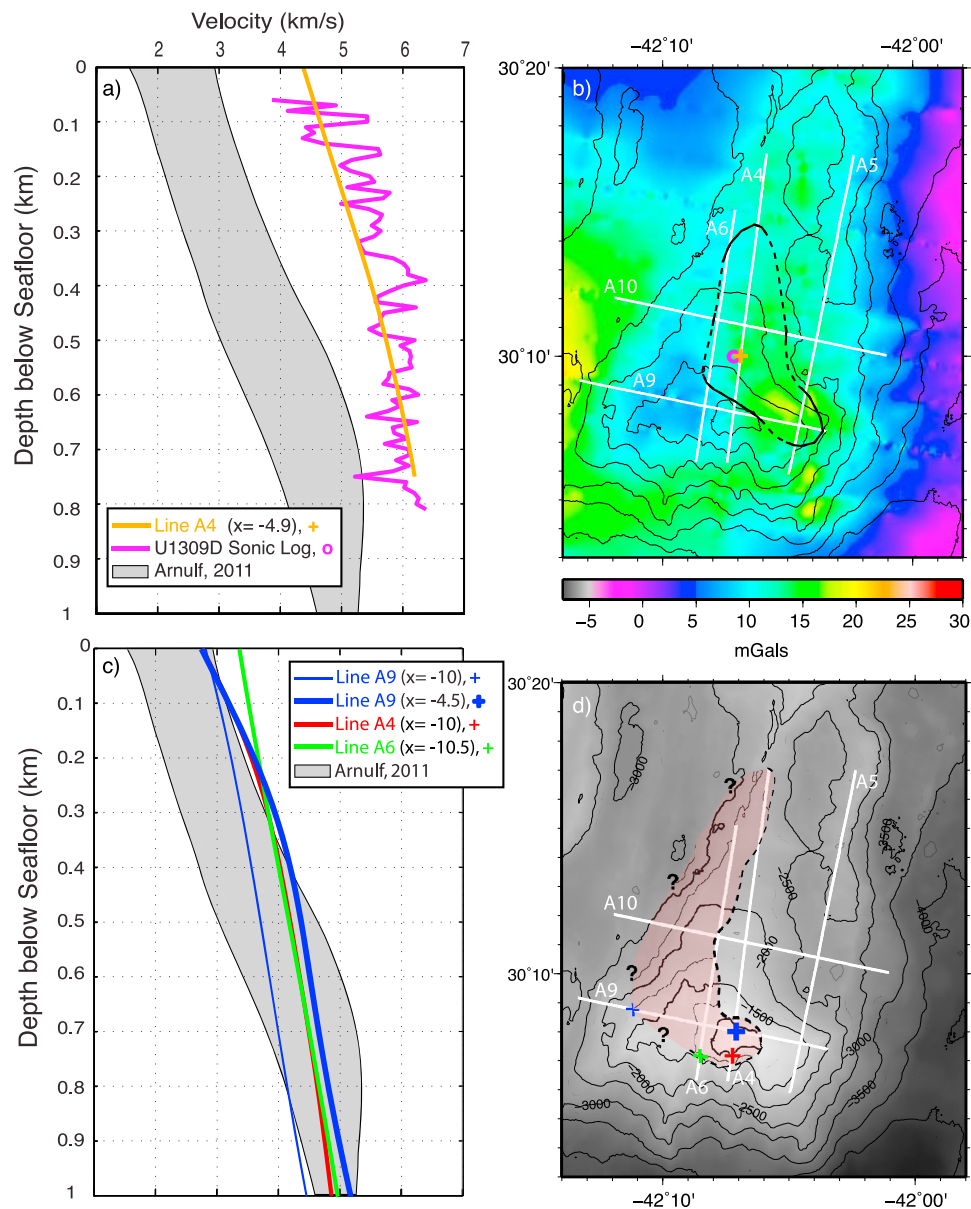


Figure 8. Representative vertical velocity profiles of (a) High Velocity Body (HVB), and (c) Intermediate-Valued Velocity Layer (IVVL). Gray shaded region is range of young Atlantic crustal velocities. Magenta curve is sonic log velocities at IODP Hole U1309D, 10 meter running average. (b) Residual Bouguer gravity anomaly (topography, intracrustal interface, and lithospheric cooling corrections made) with surface projection of the lateral extent of the HVB. Solid outline indicates boundary of HVB based on the profiles, dashed outline indicates interpolation between profiles and is guided by gravity contours. Depth to HVB varies slightly within the region. Hole U1309D and location of A4 velocity profile in Figure 8a, are noted by magenta circle and orange plus, respectively. Thin black contours show seafloor depth at 500 m contour interval. (d) Bathymetry with surface projection of the lateral extent of the IVVL. Grayshade increases with depth from shallowest contour (1000 m) with a 250 m contour interval. Colored pluses show locations of profiles in Figure 8c. Projections in Figures 8b and 8d are based on locations in models with 1D velocity structure characteristic of these regimes.

from extrusive velocity values (Figure 7b). Characteristics of the Intermediate-Valued Velocity Layer (IVVL) fit within the bounds of typical young Atlantic crustal velocities and gradients [White et al., 1992] but have surface velocities slightly higher than

what we now know layer 2A velocities to be (Figure 8c) [Hussenoeder et al., 2002; Arnulf et al., 2011; Arnulf, 2011]. The properties of these packages could indicate a crustal section composed of basalt atop either sheeted dikes [Spudich and Orcutt,

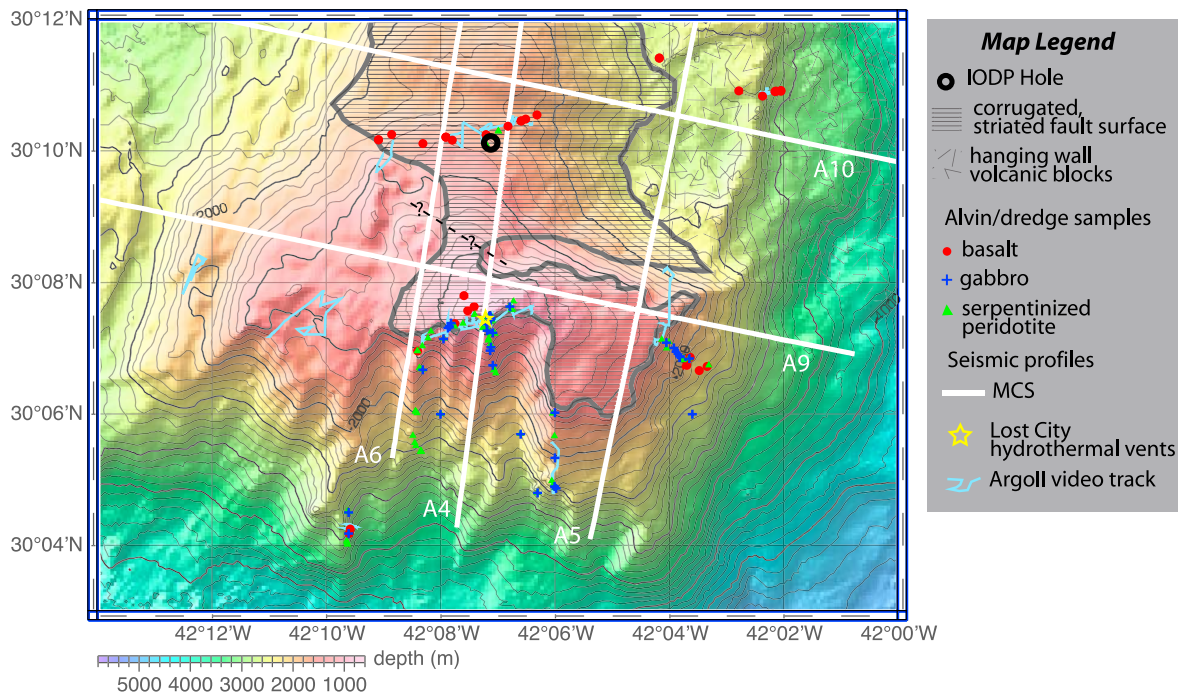


Figure 9. Map view of Atlantis Massif showing extent of corrugations, IODP Hole U1309D, sample lithology, and MCS lines. Dashed black line represents subsurface location of possible boundary between Central Dome and Southern Ridge as described in section 4.5. Modified from *Blackman et al.* [2011].

1980] or highly serpentinized harzburgite. This is based on groundtruth observations (Figure 9) and on surface velocities in the upper couple hundred meters. The projection of the spatial extent of the IVVL, inferred from our seismic results, onto the seafloor of the massif is shown in Figure 8d.

[47] The strike-parallel lines A4 and A6 show that the Southern Ridge and the northernmost 2–5 km of these two profiles are comprised of IVVL packages: 2.7–4 km/s at the seafloor increasing to >5.5 km/s at the base of the coverage (1.2–1.7 km; Figures 6a and 6b). Submersible dives on the South Wall [Blackman et al., 2002; Kelley et al., 2005; Boschi et al., 2006] recovered many samples of mostly serpentinized harzburgite and lesser gabbros near regions of IVVL velocities. On the Southern Ridge, situated atop IVVL velocities, is the Lost City Hydrothermal Field with a known serpentinite host rock composition [Kelley et al., 2001; Früh-Green et al., 2003; Kelley et al., 2005]. In addition, velocities of the IVVL are significantly faster than those observed along line A5 in the hanging wall and line A8 in the volcanic conjugate crust (Figure 7b), which suggest that they represent lithologies different from extrusive volcanics. We thus equate this IVVL zone with the intermediate V2 velocities of Canales et al. [2008] and attribute

them to lithology dominated by serpentinite on the South Wall and western and central Southern Ridge.

[48] Seismic velocities of variably altered, hand-sample-size serpentinite from the Mid-Atlantic Ridge at Kane Fracture Zone (MARK), vicinity of the Kane OCC, are presented by Miller and Christensen [1997]. For <90% alteration, measured velocities exceed those we equate with serpentinite. We note, though, that measurements on the MARK samples were made at confining pressures of 200 MPa, corresponding to conditions in the lower crust or upper mantle and ensuring the closure of microcracks within the samples. Confining pressures in the upper kilometer of the Southern Ridge are between ~10–40 MPa. At these pressures, the presence of open microcracks can reduce velocities by up to ~0.5 km/s, allowing our measurements to be consistent with smaller degrees of serpentinization. Moreover, *in situ* velocities measured by seismic waves may also be affected by large scale fracturing or by the mixture of rock compositions found at the Southern Ridge (Figure 9) [Blackman et al., 2002]. These factors cause a reduction in the seismic velocity of the IVVL compared to the serpentinite measurements of Miller and Christensen [1997].

4.2.3. Deformed Sheath Hypothesis

[49] The deformed, altered sheath hypothesis [Ildefonse *et al.*, 2007] of OCC formation can be analyzed in context of the seismic velocity models presented here. This hypothesis proposes a strong intrusive core surrounded by a sheath of weakened, serpentinized mantle rock where strain-localization and slip were concentrated during detachment fault initiation. Our models and the drilling results [Blackman *et al.*, 2011] show that mafic intrusions are present in the upper ~ 1.5 km of Atlantis Massif. This requires that these high velocity body(ies) were somehow exhumed from their originally deeper intrusion level, consistent with the deformed sheath hypothesis. The Ildefonse *et al.* [2007] model requires mafic intrusions at the core of an OCC, but it is unclear whether it requires a centrally located pluton or one skewed toward the breakaway or terminus, as observed from our models. We also observe, at least in the Southern Ridge, surface serpentinites and a velocity profile that is consistent with a deformed altered sheath. Shear zones are observed within this serpentinized material [Schroeder and John, 2004; Karson *et al.*, 2006] where some slip occurred that is consistent with the prediction of Ildefonse *et al.* [2007]. Our results do not provide enough information to definitively discern whether or not a serpentinized sheath of material encompassed the entire massif during its initial formation. If it existed, a sheath of such extent could have significantly thinned during fault displacement or been rafted away with the hanging wall. Our seismic velocity models are nevertheless consistent with the deformed, altered sheath mechanism for fault initiation and slip.

4.2.4. Outward-Facing Western Slope

[50] Additional low velocities are observed on the western outward-facing slope of the massif located west of $x = -10$ km in profiles A9 and A10 (Figures 6d and 6e). These velocities are similar to the IVVL but notably have lower velocity gradients in the upper ~ 500 meters (Figure 8c, line A9 at $x = -10$ km versus line A9 at $x = -4.5$ km and line A4 at $x = -10$ km). In contrast, the velocity-depth profile from line A6 in IVVL velocities (Figure 8c) shows a similar velocity gradient to the outward-facing slope velocities, but the overall velocities are higher. This apparent similarity in gradient is attributed to the inability to resolve the shallowest low velocity layer on line A6 as discussed previously. Preliminary 3D inversions, however, are better able to image a low velocity cap over line A6

further distinguishing it from the outward-facing slope velocity gradients.

[51] The outward-facing slope is interpreted as the location of transition into more normal upper crust and probably has an extrusive volcanic top layer. The velocities and gradients are similar to the young Atlantic crustal velocity structure of Arnulf [2011]. This interpretation is consistent with the volcanic ridge described by Smith *et al.* [2006, 2008]. Volcanic terrain was imaged in Argo-II video near this area ($\sim 30^{\circ}08.25'N$, $\sim 42^{\circ}12.5'W$ in Figure 9) [Blackman *et al.*, 2002] and a gravity deficit compared to the surrounding residual Bouguer anomaly points toward the presence of upper crustal rock (Figure 8b) [Blackman *et al.*, 2008]. This interpretation of upper crustal composition requires that the breakaway of the OCC is near $x = -10$ km in model space on line A9 and is as far east as $x = -7$ km on line A10, which is near the location of the breakaway defined by Tucholke *et al.* [1998] and Canales *et al.* [2008], in 1.8–1.9 Ma crust (based on magnetic anomalies by Sempéré *et al.* [1995]); this is very close to the western edge of the Southern Ridge.

4.2.5. Volcanic Hanging Wall

[52] The lowest velocity structure (observed only in line A5 hanging wall and line A8 conjugate crust) most likely composes basalts (Figures 6c and 6f). Rock samples obtained from near where profile A10 crosses these lowest velocities on line A5 consist entirely of basalt. Side-scan images, video, and submersible mapping record pillow basalts and hummocky volcanic structures at the surface in this area of the massif [Blackman *et al.*, 1998, 2002], in support of our interpretation of extrusive volcanic composition. Likewise, seafloor morphology and limited side-scan sonar tracks on the eastern flank of the ridge axis suggest an extrusive volcanic lithology [Blackman *et al.*, 1998].

4.2.6. Fresh Mantle

[53] Nowhere in our coverage of Atlantis Massif are mantle velocities of 8 km/s or greater observed. An OBS refraction study analyzed deeper velocity structure, to 7 km in parts, and precludes fresh mantle velocities at depths shallower than 4.5 km bsf within the Central Dome of the massif [Blackman and Collins, 2010]. The lack of evidence for fresh mantle rocks does not preclude the presence of ultramafic rocks within the massif with velocities lower than 8 km/s due either to cracks and fractures or to alteration. Indeed, as discussed

previously, we believe significant portions of the Southern Ridge are composed of serpentinite.

4.3. Correlation of Corrugations and Velocity Structure

[54] Our observations indicate that surface corrugations and striations, a defining morphologic feature of OCCs [Cann *et al.*, 1997], are present on the massif surface nearly everywhere that unusually high subsurface velocities are present (Figure 9). Corrugations and surface striations are also present in some areas of lower velocities not indicative of extrusive volcanic lithology. The central portion of line A9 and the southern portions of lines A4 and A6, all on the Southern Ridge, show corrugations capping a region where we determine subsurface IVVL velocities (Figure 9). Also shown by Figure 9, along line A10 west of the line A6 intersection, lithospheric velocities decrease steadily across a region where corrugations have been mapped [Blackman *et al.*, 2002]. These observations reinforce the general correlation between corrugations and intrusive material with high seismic velocity structure as implied by Tucholke *et al.* [2008], but the correspondence is not exclusive. We also note that seafloor corrugations can cap material that we infer to be altered ultramafic rock.

4.4. Correlation With Gravity Structure

[55] Our seismic models and our lithologic inferences qualitatively match the preferred residual Bouguer gravity anomaly (RBA) model of Blackman *et al.* [2008]. In their preferred model, the density contrast at the water/crustal interface is 1600 kg/m^3 , and that of the upper crust/lower crust boundary is 300 kg/m^3 . The lower crust, assumed to have a density of 2900 kg/m^3 based on the average density of material from Hole U1309D [Blackman *et al.*, 2006], shoals almost to the seafloor in the central portion of the massif in this model. Despite the removal of a lower crustal component, a positive RBA ($\sim 15\text{--}20 \text{ mgal}$) exists over the eastern Central Dome and Southern Ridge (Figure 8b).

[56] The skewness of the positive gravity anomaly correlates well with the distribution of the high velocity sections in our models that we have interpreted as a gabbroic body(ies). In the Southern Ridge, we confirm that the positive anomaly in the preferred gravity model most likely represents an additional mafic component in the east of the Southern Ridge suggesting that it is composed of material similar to the Central Dome based on the similar magnitude of anomaly in these areas. This

argument is in agreement with the model of *Ildefonse et al.* [2007].

[57] A relative mass deficit shown by the RBA (Figure 8b) over the central and western Southern Ridge is a positive anomaly of smaller magnitude ($\sim 5 \text{ mgal}$) compared to the larger positive anomaly ($\sim 15\text{--}20 \text{ mgal}$) modeled in the Central Dome and eastern Southern Ridge [Blackman *et al.*, 2008]. This $\sim 5 \text{ mgal}$ anomaly in the western and central Southern Ridge could occur due to remaining material of lower density, possibly of serpentinite or porous mafic composition. This is consistent with our interpretation of a transition to classical crustal composition on the outward-facing slope of Atlantis Massif.

4.5. Magmatism and Gabbroic Bodies at Atlantis Massif

[58] The high velocity body(ies) with $4.5\text{--}5.5 \text{ km/s}$ at the seafloor and extending throughout the MCS refraction depth coverage are interpreted as a gabbroic body or bodies consistent with IODP drilling at Atlantis Massif [Blackman *et al.*, 2006] and at other OCCs [Dick *et al.*, 2000; MacLeod *et al.*, 2002; Kelemen *et al.*, 2004]. This lithology indicates that plutons were present or that magmatism was active at the ridge during the initiation of Atlantis Massif, and recent models [Buck *et al.*, 2005; Tucholke *et al.*, 2008; Olive *et al.*, 2010] would predict that intermediate levels of magmatism accounting for $\sim 30\text{--}50\%$ of lithospheric accretion were characteristic of the period between initiation and termination of this core complex. This body(ies) would have been emplaced into a mainly peridotitic host rock exhumed during the dominantly extensional phases of lithospheric accretion.

[59] The shape of the high velocity anomaly at Atlantis Massif (Figure 8b) suggests a magmatic source that evolved through time and space, rather than remaining in a constant location over the formation period of the OCC. The body(ies) is centered beneath the Central Dome to the north but it comprises only the eastern flank of the Southern Ridge to the south; there is a $\sim 3.5 \text{ km}$ difference in the position of high velocities in the spreading direction between the two spreading-parallel profiles (Figures 6d and 6e). Although we interpolate a single boundary for the HVB between seismic profiles (Figure 8b), we cannot definitively conclude that the Central Dome and Southern Ridge gabbroic bodies are continuous as our profiles are

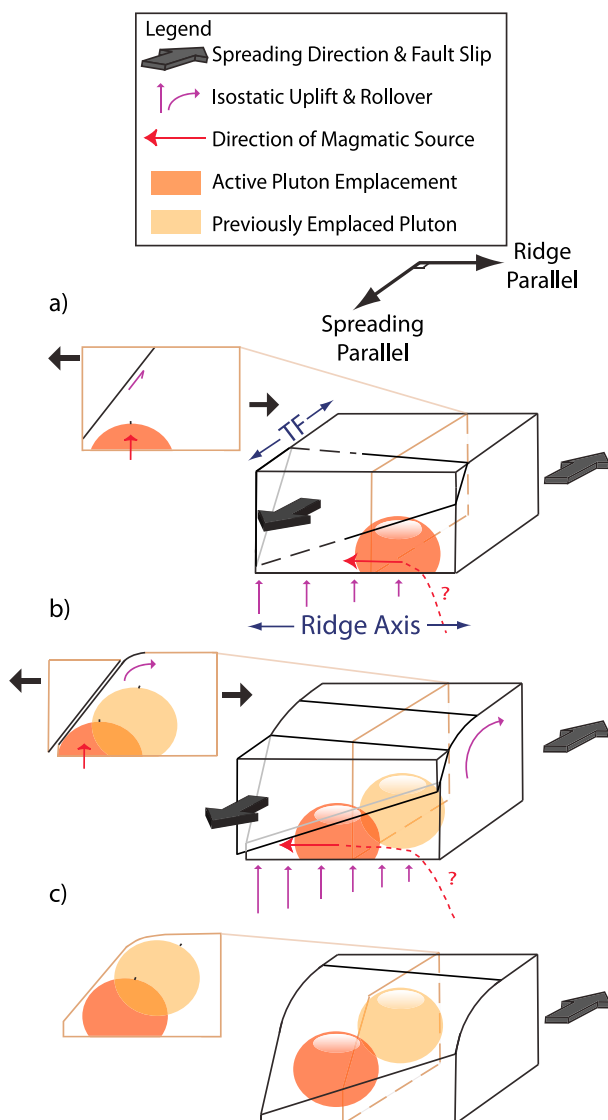


Figure 10. Block diagrams and cross-sections illustrating the emplacement history of the plutonic core of Atlantis Massif. (a) Magmatic injection initiates at the north end of the current extent of Atlantis Massif. Strain localizes at the margin of the resultant pluton forming a detachment fault in the north. (b) As the first area of injection is rafted off axis by spreading, the injection source and detachment fault propagate to the south. Isostatic forces are greater in the south due to the southeast dip of the detachment fault. (c) The final geometry of the plutonic core seen at present-day Atlantis Massif.

spaced too far apart to observe a boundary between gabbroic bodies, if one exists.

[60] Based on the velocity models, a transition between the Central Dome and Southern Ridge may occur at about $x = -7.5$ km along line A4 and $x = -6.5$ km on A6 (Figure 9, dashed line), where the velocity difference from the starting model

changes from positive to negative (Figures 5a and 5b). Following the interpretation of *Canales et al.* [2008], this may support the inference of *Karson et al.* [2006] that the Central Dome and Southern Ridge are made of two distinct crustal blocks. However, there is no clear surface-trace of a lateral fault in that region. We note that a slight difference in the starting model could change the location of a gradual transition from positive to negative velocity anomalies as seen in line A6 (Figure 5a), but would not affect the location of the high gradient transition like that in line A4 (Figure 5b).

[61] Systematic analysis of the IODP drill core U1309D [*John et al.*, 2009] suggests that the HVB, at least in the Central Dome region, is composed of a series of sills injected individually and age dating confirms this [*Grimes et al.*, 2008]. From our data, it is not possible to determine if the magmatic source remained constant, injecting material steadily for the duration of its evolution, or if it comprised discrete magmatic pulses forming a main body or section of bodies first in the north, then subsequently in the south. Whether this is the case or not does not affect the main conclusions of our model.

[62] We propose an evolutionary history of the magmatic source based on the simplest explanation constrained by the data: the magmatic source underwent continuous emplacement throughout OCC formation building up to two discrete ~ 5 – 10 km-scale bodies, and the rates of along axis movement of the source and of seafloor spreading (rates based on length and age of Atlantis Massif, and based on dating by *Grimes et al.* [2008]) controlled the shape of the resultant pluton(s). Thus, as the magmatic source moved south along the ridge axis, the continuous spreading of the plates rafted portions of the body off-axis to greater distances in the north than in the south (Figure 10). This hypothesis predicts that a diagonal or curved gabbroic body(ies) underlies Atlantis Massif as inferred from the seismic models and residual gravity anomaly [*Blackman et al.*, 1998, 2008].

[63] At time t_1 , magmatic emplacement takes place at the ridge in the along-axis position of the present-day Central Dome (Figure 10a). As the hot pluton contributes to the buoyancy forces experienced by the lithosphere, it begins to be spread off axis. Meanwhile, the magma source migrates southward where it injects a second pluton at time t_2 in the along-axis location of the present-day Southern Ridge (Figure 10b). The source could just as likely undergo continuous emplacement during southward migration, but for a simplified time series, we

illustrate and describe the process with two discrete bodies. This second body emplaced at time t_2 is uplifted and rafted off axis in the same way as the first pluton. At time t_3 , two plutons exist (or one continuous pluton) with the northern body farther from the spreading axis and the southern body closer (Figure 10c).

[64] It is prudent to note that a magma source that dips from north to south in the lithosphere could create a similar geometry. This, however, would not be consistent with the sill injection mechanism proposed by *Grimes et al.* [2008] which requires more recent injections to occur higher in the lithosphere than the initial magmatic episode. Our model of a propagating source does not confine the depth of the magmatic injections, which may be inserted directly into the footwall [*Tucholke et al.*, 2008].

4.6. Implications of the Magmatic History for Detachment Fault Formation and Unroofing Mechanism

[65] Many studies have argued that magmatism is an important factor in the formation of detachment faults [*Dick et al.*, 2002; *Buck et al.*, 2005; *Ildefonse et al.*, 2007; *Tucholke et al.*, 2008; *Olive et al.*, 2010]. The existence of plutonic bodies at Atlantis Massif confirms the presence of magmatism. *Ildefonse et al.* [2007] propose a model where detachment faults form as strain nucleates in the weakened material at the edges of a magmatic body emplaced into ultramafic host rock. We favor this hypothesis for the nucleation of the detachment fault because it is consistent with the near surface exposure of gabbroic bodies and the observed morphology and rock types at Atlantis Massif [*Blackman et al.*, 2011] and draws support from alteration analysis indicating that alteration to weak minerals occurred around the boundaries of magmatic injections at this OCC [*Nozaka and Fryer*, 2011].

[66] We propose a model of detachment fault formation and geometry in which a southeast dipping detachment fault formed at Atlantis Massif during, or soon after, the southward propagation of the magmatic source. The detachment nucleates at the interface between host rock and pluton [*Ildefonse et al.*, 2007], first in the north at the site of earliest emplacement. This requires a breakaway that is subparallel to the spreading ridge (Figure 11a), which is possible based on the morphology of the western flank of Atlantis Massif [*Cann et al.*, 1997; *Blackman et al.*, 1998]. Simultaneously, plate spreading and slip on the newly forming

detachment fault proceed. The fault continues to cut deeply southward into the crust at the plutonic boundary, which is deeper in the lithospheric section in the south than its concurrent position in the north where it has already undergone uplift. This process is the mechanism for formation of a southeast dipping fault that cuts deeper into the lithosphere in the south than in the north (Figures 10 and 11a). After the development of the detachment fault, plate spreading is accommodated dominantly on this fault for at least 0.2 Myr, the period of OCC formation determined by age dating conducted by *Grimes et al.* [2008] (Figure 11b). Corrugations form on the footwall marking the spreading-parallel relative motion of fault blocks during detachment slip (Figure 9) [*Cann et al.*, 1997; *Tucholke et al.*, 1998, 2008].

[67] Unroofing of the footwall to a southeast dipping detachment fault will form morphology similar to that of Atlantis Massif (Figure 1) based on an increasing north to south gradient in isostatic uplift as well as the exposure of originally deeper and more ultramafic rock in the south, where the fault cuts deeper. The amount of mass removed from above the south part of the footwall will exceed that removed from the north due to the orientation of the fault, which cuts a wedge-shaped hanging wall (Figures 10 and 11b). When an uneven mass of material is removed from the top of the fault, isostatic compensation will vary along strike (Figures 11b and 11c) causing the crust to be uplifted higher in the south than in the north (Figure 11d).

[68] The hanging wall material displaced by motion on the detachment fault, at least in part, still exists atop the northern two-thirds of Atlantis Massif. The velocities in our models suggest however, that the part of the hanging wall that once covered the Southern Ridge must have been removed by some mechanism that cannot be determined from the seismic data. Both mass wasting of the material or transfer of the southern portion of hanging wall onto the outside corner conjugate crust are possible explanations for its absence atop the massif. Exactly how much material comprised the southern section of the hanging wall is unknown. If the core pluton(s) of Atlantis Massif were emplaced into ultramafic host rock, as suggested here and by *Ildefonse et al.* [2007], a relatively lesser amount of hanging wall of dense ultramafic composition would need to be removed to account for the uplift of the Southern Ridge. Alternatively, if the pluton(s) were emplaced into normal young Atlantic crust and the hanging wall was composed of extrusive,

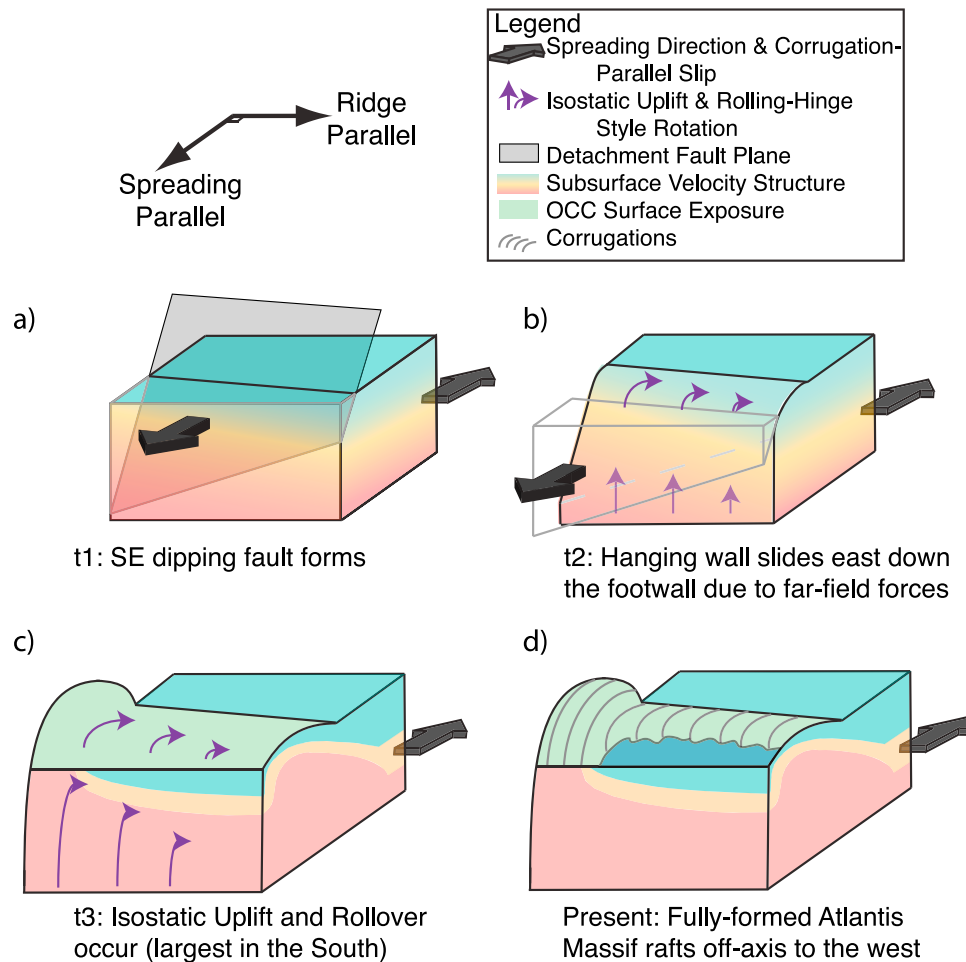


Figure 11. Sketch of faulting and uplift model. (a) At time t1: a southeast dipping detachment fault forms, creating a wedge-shaped hanging wall. (b) At time t2: the hanging wall slips down the footwall causing footwall uplift and a gradient in isostatic forces due to the uneven unloading of the footwall. (c) At time t3: Uplift of the footwall is greater in the south than in the north. (d) Present: present morphology of Atlantis Massif.

mafic material, removal of larger volumes would be required to spur uplift. We prefer the former explanation of host rock composition, where the upper crustal component tapers off and mafic/ultramafic material shoals as the segment end is approached (Figure 11a). This allows for the southern (missing) portion of hanging wall to have a denser composition than what is currently observed atop the northern two-thirds of the massif.

[69] If the southern hanging wall material was mass wasted, perhaps during uplift or flexure of the Southern Ridge, it may have disbursed throughout the local axial valley and the nodal basin. A lobe of material exists at the southeastern base of Atlantis Massif (Figure 1 at 30°05'N–30°10'N, 42°03'W) and the nodal basin, although deep, is smooth with several isolated large blocks of material at its northern edge. These features are consistent with a flow of mass wasted material. Alternatively, if the

detachment fault rooted in the axial valley, it is possible that some of the hanging wall material was transferred to the conjugate flank of the spreading axis. Results from reflection analysis of MCS profile A8 on the outside corner suggest that the upper crustal section on the conjugate flank is thicker than normal [Canales *et al.*, 2004] by ~250–500 m, supporting this conclusion.

[70] Lithologic evidence also supports the hypothesis of a southeast dipping fault cutting into ultramafic host rock. A wedge shaped hanging wall cutting deeper into the lithospheric section at one end will expose deeper, more ultramafic material at that end when isostatically uplifted. This is a possible explanation for the higher volume of serpentinized mantle rocks found on the southern end and contributes to the overall lithospheric heterogeneity of Atlantis Massif.

[71] Simple isostasy and alteration approximations are considered to test the credibility of the southeast dipping detachment fault hypothesis as it relates to the observed morphology and lithology of Atlantis Massif. *Lavier et al.* [1999], basing their model on the rolling hinge model of *Buck* [1988], predict 2600 m of footwall uplift for a detachment fault that has undergone ~ 27 km of slip, similar to one estimate of slip proposed for Atlantis Massif [*Tucholke et al.*, 1998]. We propose a combination of factors may all contribute to the >1 km of relative relief between the Southern Ridge and Central Dome: 1) greater isostatic forces acting where more overlying material has been removed from the Southern Ridge; 2) a possible spreading-parallel fault between Southern Ridge and Central Dome [e.g., *Karson et al.*, 2006] with some normal motion; and 3) expansion from increased degree of serpentinization of deeper, more olivine-rich material in the south. Gravity results show that the region of Atlantis Massif is not completely isostatically compensated [*Blackman et al.*, 1998, 2008], indicating that additional uplift may occur over time.

[72] Spreading-parallel faulting was suggested by *Karson et al.* [2006] to have occurred between a Southern Ridge of serpentinite composition and a gabbroic Central Dome. While our results indicate that the gabbroic lithology occurs in several portions of Atlantis Massif, it is possible that a spreading-parallel fault exists between these two morphologic components, perhaps between two discrete gabbroic bodies. Normal faulting of this orientation at the northern extreme of the Southern Ridge (e.g. $30^{\circ}08.5'N$) may provide a mechanism for increased uplift in the south. Assuming a fault of this orientation and location, and depending on the degree of coupling across the transform fault and the possible presence of transform-dipping faulting, an additional ~ 650 – 1550 m of uplift may be achieved on the Southern Ridge [*Baines et al.*, 2003].

[73] Likewise, a 20–30% volumetric expansion associated with the olivine to serpentinite reaction (per cent volumetric expansion determined for samples from Kane OCC) [*Karson and Lawrence*, 1997] may contribute to the increased uplift of the Southern Ridge. A fault cutting several kilometers deeper into the lithosphere on one side may bring seawater into contact with material of high olivine content. A rate of serpentinization of $1.4e-4$ km³/yr is determined for Atlantis Massif [*Früh-Green et al.*, 2003]. Using this estimate for rate of serpentinization over the last 1.5 Ma, ~ 210 km³ of serpentinite would have been produced since

Atlantis Massif initiated. This would contribute to a volumetric expansion of ~ 42 – 63 km³ during the history of Atlantis Massif, contributing to overall massif uplift, the majority of which would occur in the Southern Ridge where olivine content is highest due to the fault cutting deeper into the lithospheric section in this area. *O'Hanley* [1992] notes that a serpentinization-induced volumetric expansion of 25% leads to a linear expansion of 8%. This would contribute to ~ 70 m increase in topography on the entire area of the Southern Ridge if we assume that all serpentinization occurs there. We conclude that the dipping detachment fault and isostatic uplift are the primary controls on the morphologic and lithologic structure of Atlantis Massif (Figure 11d).

5. Conclusion

[74] Tomographic inversion of multichannel seismic data processed with the SOBE downward continuation technique allows for dense and detailed coverage of the upper ~ 1.5 km of structure within the smooth, high-relief Atlantis Massif oceanic core complex and its conjugate crust. Independent constraints from rock samples and gravity modeling allow us to infer geologic structure from our tomographic models. The general consistency between rock sample type and the velocities obtained indicate that SOBE processed MCS data are an effective and valuable method for guiding geologic interpretation, by exposing shallow turning arrivals for picking and inclusion in the inversion process.

[75] A broad range of velocity structure regimes is observed in our results and the lateral heterogeneity within the seismic structure is great. Values larger than 5.5 km/s occur just below the seafloor in some areas and are interpreted as gabbroic rock based on velocity, velocity gradient, gravity, and deep drilling results. This is consistent with inferences drawn by *Canales et al.* [2008]. Much lower velocity packages, with velocity-depth profiles similar to those of young Atlantic crust [*Arnulf et al.*, 2011; *Arnulf*, 2011], are present in the models at lateral offsets as little as ~ 1 – 2 km from the higher gabbroic velocities (line A9, 5.5 km/s to 2 km/s over 1.5 km). These lower velocities, termed here the IVVL, are interpreted as highly serpentinized periodite on the Southern Ridge based on groundtruth and the considerable difference in velocity structure between these velocities and the velocities of lines A5 and A8 (hanging wall and conjugate crust, respectively), which are of extrusive basaltic composition. The outward-facing slope on the west of the massif is interpreted to contain at least some crust of

extrusive volcanics based on the correlation of 1D velocity structure with that of typical young Atlantic crust, the volcanic terrain imaged by Argo-II, and a gravity deficit. Vertical velocity gradients within the upper ~ 1.5 km range from $<1 \text{ s}^{-1}$ to $>3 \text{ s}^{-1}$, contributing to the overall heterogeneity of the massif structure.

[76] We infer that this oceanic core complex is composed of a dominantly gabbroic core, with a likely persisting sheath of serpentinized peridotite in some areas, and volcanic material on the eastern OCC flank and outward-facing slope. This interpretation is most consistent with the model proposed by *Ildefonse et al.* [2007] of a pluton emplaced in a peridotite host rock, followed by seawater alteration and strain localization within the peridotite causing detachment fault formation and slip, leading to an OCC with a mafic core surrounded by serpentinite. The presence of low velocities representative of volcanics on the outward-facing slope near the breakaway is consistent with a tilted basaltic ridge that emerges at the onset of OCC formation [*Smith et al.*, 2006], while the low-velocity volcanic material on the eastern ridge flank is a remnant of the once overlying hanging wall.

[77] The gabbroic composition of the core of Atlantis Massif indicates that magmatism was active to some extent during OCC formation. Based on the shape of the plutonic core inferred from our models, we hypothesize that a southward propagating magmatic source is responsible for emplacement and has created a curved gabbroic body(ies). Based on the 30–50% magmatic emplacement to tectonic extension ratio [*Buck et al.*, 2005; *Tucholke et al.*, 2008; *Olive et al.*, 2010] predicted for the initiation of a detachment fault and the strain localization model of *Ildefonse et al.* [2007], it follows that a southeast dipping detachment fault may have formed above the upper edge of the gabbroic pluton as the source traveled along axis. A fault with this orientation, cutting deeply into the ultramafic lithosphere in the south, is consistent with both the morphology and lithology of the present-day Atlantis Massif.

Acknowledgments

[78] The authors would like to offer sincere thanks to associate editor M. Cheadle, reviewer H. Van Avendonk, and an anonymous reviewer for comments and suggestions that greatly improved the paper. We also appreciate the use of the Generic Mapping Tools (GMT) program [*Wessel and Smith*, 1991]. NSF support was provided via grant OCE-0927442.

References

- Allerton, S., J. Escartín, and R. Searle (2000), Extremely asymmetric magmatic accretion of oceanic crust at the ends of slow-spreading ridge segments, *Geology*, *28*(2), 179–182, doi:10.1130/0091-7613(2000)28<179:EAMAO>?2.0.CO;2.
- Arnulf, A. F. (2011), Layer 2A structure beneath the Lucky Strike volcano, Mid-Atlantic Ridge, from high-resolution tomography and full waveform inversion, PhD thesis, Inst. Phys. du Globe de Paris, Paris.
- Arnulf, A., S. Singh, A. Harding, G. Kent, and W. Crawford (2011), Strong seismic heterogeneity in layer 2a near hydrothermal vents at the Mid-Atlantic Ridge, *Geophys. Res. Lett.*, *38*, L13320, doi:10.1029/2011GL047753.
- Baines, A., M. Cheadle, H. Dick, A. Scheirer, B. John, N. Kusznir, and T. Matsumoto (2003), Mechanism for generating the anomalous uplift of oceanic core complexes: Atlantis Bank, Southwest Indian Ridge, *Geology*, *31*(12), 1105–1108, doi:10.1130/G19829.1.
- Blackman, D., and J. Collins (2010), Lower crustal variability and the crust/mantle transition at the Atlantis Massif oceanic core complex, *Geophys. Res. Lett.*, *37*, L24303, doi:10.1029/2010GL045165.
- Blackman, D., J. Cann, B. Janssen, and D. Smith (1998), Origin of extensional core complexes: Evidence from the Mid-Atlantic Ridge at Atlantis Fracture Zone, *J. Geophys. Res.*, *103*(B9), 21,315–21,333, doi:10.1029/98JB01756.
- Blackman, D., et al. (2002), Geology of the Atlantis Massif (Mid-Atlantic Ridge, 30°N): Implications for the evolution of an ultramafic oceanic core complex, *Mar. Geophys. Res.*, *23*(5), 443–469, doi:10.1023/B:MARI.0000018232.14085.75.
- Blackman, D., B. Ildefonse, B. John, Y. Ohara, D. Miller, and C. MacLeod (2006), Expedition 304/305 scientists, *Proc. Integrated Ocean Drill. Program*, *304/305*, doi:10.2204/iodp.sp.304305.2005.
- Blackman, D., G. Karner, and R. Searle (2008), Three-dimensional structure of oceanic core complexes: Effects on gravity signature and ridge flank morphology, Mid-Atlantic Ridge, 30°N, *Geochem. Geophys. Geosyst.*, *9*(6), Q06007, doi:10.1029/2008GC001951.
- Blackman, D., et al. (2011), Drilling constraints on lithospheric accretion and evolution at Atlantis Massif, Mid-Atlantic Ridge 30°N, *J. Geophys. Res.*, *116*, B07103, doi:10.1029/2010JB007931.
- Boschi, C., G. Früh-Green, A. Delacour, J. Karson, and D. Kelley (2006), Mass transfer and fluid flow during detachment faulting and development of an oceanic core complex, atlantis massif (MAR 30°N), *Geochem. Geophys. Geosyst.*, *7*, Q01004, doi:10.1029/2005GC001074.
- Buck, W. (1988), Flexural rotation of normal faults, *Tectonics*, *7*(5), 959–973, doi:10.1029/TC007i005p00959.
- Buck, W., L. Lavier, and A. Poliakov (2005), Modes of faulting at mid-ocean ridges, *Nature*, *434*(7034), 719–723, doi:10.1038/nature03358.
- Canales, J., R. Detrick, J. Lin, J. Collins, and D. Toomey (2000a), Crustal and upper mantle seismic structure beneath the rift mountains and across a nontransform offset at the Mid-Atlantic Ridge (35°N), *J. Geophys. Res.*, *105*(B2), 2699–2719, doi:10.1029/1999JB900379.
- Canales, J., J. Collins, J. Escartín, and R. Detrick (2000b), Seismic structure across the rift valley of the mid-atlantic ridge at 23°20′N (MARK area): Implications for crustal accretion processes at slow spreading ridges, *J. Geophys. Res.*, *105*(B12), 28,411–28,425, doi:10.1029/2000JB900301.



- Canales, J., B. Tucholke, and J. Collins (2004), Seismic reflection imaging of an oceanic detachment fault: Atlantis Megamullion (Mid-Atlantic Ridge, 30°10'N), *Earth Planet. Sci. Lett.*, *222*(2), 543–560, doi:10.1016/j.epsl.2004.02.023.
- Canales, J., R. Detrick, S. Carbotte, G. Kent, J. Diebold, A. Harding, J. Babcock, M. Nedimovic, and E. Van Ark (2005), Upper crustal structure and axial topography at intermediate spreading ridges: Seismic constraints from the southern Juan de Fuca Ridge, *J. Geophys. Res.*, *110*, B12104, doi:10.1029/2005JB003630.
- Canales, J., B. Tucholke, M. Xu, J. Collins, and D. DuBois (2008), Seismic evidence for large-scale compositional heterogeneity of oceanic core complexes, *Geochem. Geophys. Geosyst.*, *9*, Q08002, doi:10.1029/2008GC002009.
- Cann, J., D. Blackman, D. Smith, E. McAllister, B. Janssen, S. Mello, E. Avgerinos, A. Pascoe, and J. Escartin (1997), Corrugated slip surfaces formed at ridge-transform intersections on the Mid-Atlantic Ridge, *Nature*, *385*(6614), 329–332, doi:10.1038/385329a0.
- Cannat, M. (1993), Emplacement of mantle rocks in the seafloor at mid-ocean ridges, *J. Geophys. Res.*, *98*(B3), 4163–4172, doi:10.1029/92JB02221.
- Cannat, M., D. Sauter, V. Mendel, E. Ruellan, K. Okino, J. Escartin, V. Combier, and M. Baala (2006), Modes of seafloor generation at a melt-poor ultraslow-spreading ridge, *Geology*, *34*(7), 605–608, doi:10.1130/G22486.1.
- Christeson, G., G. Purdy, and G. Fryer (1994), Seismic constraints on shallow crustal emplacement processes at the fast spreading East Pacific Rise, *J. Geophys. Res.*, *99*(B9), 17,957–17,973, doi:10.1029/94JB01252.
- Collins, J., D. Blackman, A. Harris, and R. Carlson (2009), Seismic and drilling constraints on velocity structure and reflectivity near IODP Hole U1309D on the central dome of Atlantis Massif, Mid-Atlantic Ridge 30°N, *Geochem. Geophys. Geosyst.*, *10*(1), Q01010, doi:10.1029/2008GC002121.
- Detrick, R., H. Needham, and V. Renard (1995), Gravity anomalies and crustal thickness variations along the Mid-Atlantic Ridge between 33°N and 40°N, *J. Geophys. Res.*, *100*(B3), 3767–3787, doi:10.1029/94JB02649.
- Dick, H., et al. (2000), A long in situ section of the lower ocean crust: Results of ODP leg 176 drilling at the Southwest Indian Ridge, *Earth Planet. Sci. Lett.*, *179*(1), 31–51, doi:10.1016/S0012-821X(00)00102-3.
- Dick, H., et al. (2002), Primary silicate mineral chemistry of a 1.5-km section of very slow spreading lower ocean crust: ODP hole 735b, Southwest Indian Ridge, *Proc. Ocean Drill. Program Sci. Results*, *176*, 1–61, doi:10.2973/odp.proc.sr.176.001.2002.
- Dick, H., M. Tivey, and B. Tucholke (2008), Plutonic foundation of a slow-spreading ridge segment: Oceanic core complex at Kane Megamullion, 23°30' N, 45°20' W, *Geochem. Geophys. Geosyst.*, *9*, Q05014, doi:10.1029/2007GC001645.
- Escartin, J., C. Mével, C. MacLeod, and A. McCaig (2003), Constraints on deformation conditions and the origin of oceanic detachments: The Mid-Atlantic Ridge core complex at 15°45'N, *Geochem. Geophys. Geosyst.*, *4*(8), 1067, doi:10.1029/2002GC000472.
- Escartin, J., D. Smith, J. Cann, H. Schouten, C. Langmuir, and S. Escrig (2008), Central role of detachment faults in accretion of slow-spreading oceanic lithosphere, *Nature*, *455*, 790–794, doi:10.1038/nature07333.
- Früh-Green, G., D. Kelley, S. Bernasconi, J. Karson, K. Ludwig, D. Butterfield, C. Boschi, and G. Proskurowski (2003), 30,000 years of hydrothermal activity at the Lost City Vent Field, *Science*, *301*(5632), 495–498, doi:10.1126/science.1085582.
- Grimes, C., B. John, M. Cheadle, and J. Wooden (2008), Protracted construction of gabbroic crust at a slow spreading ridge: Constraints from ²⁰⁶Pb/²³⁸U zircon ages from Atlantis Massif and IODP hole U1309D (30°N, MAR), *Geochem. Geophys. Geosyst.*, *9*, Q08012, doi:10.1029/2008GC002063.
- Harding, A., G. Kent, and J. Orcutt (1993), A multichannel seismic investigation of upper crustal structure at 9°N on the east Pacific Rise: Implications for crustal accretion, *J. Geophys. Res.*, *98*(B8), 13,925–13,944, doi:10.1029/93JB00886.
- Harding, A., G. Kent, D. Blackman, S. Singh, and J. Canales (2007), A new method for MCS refraction data analysis of the uppermost section at a Mid-Atlantic Ridge core complex, in *Eos Trans. AGU*, *88*(52), Fall Meet. Suppl., Abstract S12A-03.
- Hooft, E., R. Detrick, D. Toomey, J. Collins, and J. Lin (2000), Crustal thickness and structure along three contrasting spreading segments of the Mid-Atlantic Ridge, 33.5–35°N, *J. Geophys. Res.*, *105*(B4), 8205–8226, doi:10.1029/95JB02502.
- Hussenoeder, S., G. Kent, and R. Detrick (2002), Upper crustal seismic structure of the slow spreading Mid-Atlantic Ridge, 35°N: Constraints on volcanic emplacement processes, *J. Geophys. Res.*, *107*(B8), 2156, doi:10.1029/2001JB001691.
- Ildefonse, B., et al. (2007), Oceanic core complexes and crustal accretion at slow-spreading ridges, *Geology*, *35*(7), 623–626, doi:10.1130/G23531A.1.
- John, B., M. Cheadle, J. Gee, C. Grimes, A. Morris, and N. Pressling (2009), Data report: Spatial and temporal evolution of slow spread oceanic crust—Graphic sections of core recovered from IODP hole U1309D, Atlantis Massif, 30°N, MAR (including Pb/U zircon geochronology and magnetic remanence data), *Proc. Ocean Drill. Program*, *304/305*, doi:10.2204/iodp.proc.304305.205.2009.
- Karson, J. (1999), Geological investigation of a lineated massif at the Kane Transform Fault: Implications for oceanic core complexes, *Philos. Trans. R. Soc. London, Ser. A*, *357*(1753), 713–740, doi:10.1098/rsta.1999.0350.
- Karson, J., and R. Lawrence (1997), Tectonic setting of serpentinite exposures on the western median valley wall of the MARK area in the vicinity of site 920, *Proc. Ocean Drill. Program*, *153*, 5–22, doi:10.2973/odp.proc.sr.153.001.1997.
- Karson, J., G. Früh-Green, D. Kelley, E. Williams, D. Yoerger, and M. Jakuba (2006), Detachment shear zone of the Atlantis Massif core complex, Mid-Atlantic Ridge, 30°N, *Geochem. Geophys. Geosyst.*, *7*, Q06016, doi:10.1029/2005GC001109.
- Kelemen, P., E. Kikawa, D. Miller, and Shipboard Scientific Party (2004), Leg 209 summary, *Proc. Ocean Drill. Program Initial Rep.*, *209*, doi:10.2973/odp.proc.sr.153.001.1997.
- Kelley, D., et al. (2001), An off-axis hydrothermal vent field near the Mid-Atlantic Ridge at 30°N, *Nature*, *412*, 145–149, doi:10.1038/35084000.
- Kelley, D., et al. (2005), A serpentinite-hosted ecosystem: The Lost City Hydrothermal Field, *Science*, *307*(5714), 1428–1434, doi:10.1126/science.1102556.
- Kuo, B., and D. Forsyth (1988), Gravity anomalies of the ridge-transform system in the south Atlantic between 31 and 34.5°S: Upwelling centers and variations in crustal thickness, *Mar. Geophys. Res.*, *10*(3–4), 205–232, doi:10.1007/BF00310065.
- Lavier, L., W. Roger Buck, and A. Poliakov (1999), Self-consistent rolling-hinge model for the evolution of large-offset low-angle normal faults, *Geology*, *27*(12), 1127–1130, doi:10.1130/?0091-7613(1999)?027<1127:SCRHMF>2.3.CO;2.
- Lin, J., G. Purdy, H. Schouten, J. Sempere, and C. Zervas (1990), Evidence from gravity data for focused magmatic



- accretion along the Mid-Atlantic Ridge, *Nature*, 344(6267), 627–632, doi:10.1038/344627a0.
- MacLeod, C., et al. (2002), Direct geological evidence for oceanic detachment faulting: The Mid-Atlantic Ridge, 15°45'N, *Geology*, 30(10), 879–882, doi:10.1130/0091-7613(2002)030<0879:DGEFOD>?2.0.CO;2.
- MacLeod, C., R. Searle, B. Murton, J. Casey, C. Mallows, S. Unsworth, K. Achenbach, and M. Harris (2009), Life cycle of oceanic core complexes, *Earth Planet. Sci. Lett.*, 287(3–4), 333–344, doi:10.1016/j.epsl.2009.08.016.
- McCaig, A., A. Delacour, A. Fallick, T. Castelain, and G. Fruh-Green (2010), Detachment fault control on hydrothermal circulation systems: Interpreting the subsurface beneath the TAG hydrothermal field using the isotopic and geological evolution of oceanic core complexes in the Atlantic, in *Diversity of Hydrothermal Systems on Slow Spreading Ocean Ridges*, *Geophys. Monogr. Ser.*, vol. 188, edited by P. A. Rona et al., 207–240, AGU, Washington, D. C.
- Michael, P., et al. (1994), Mantle control of a dynamically evolving spreading center: Mid-Atlantic Ridge 31–34°S, *Earth Planet. Sci. Lett.*, 121(3–4), 451–468, doi:10.1016/0012-821X(94)90083-3.
- Miller, D., and N. Christensen (1997), Seismic velocities of lower crustal and upper mantle rocks from the slow-spreading Mid-Atlantic Ridge, south of the Kane transform zone (MARK), *Proc. Ocean Drill. Program Sci. Results*, 153, 437–454, doi:10.2973/odp.proc.sr.153.043.1997.
- Morris, E., and R. Detrick (1991), Three-dimensional analysis of gravity anomalies in the MARK area, Mid-Atlantic Ridge 23°N, *J. Geophys. Res.*, 96(B3), 4355–4366, doi:10.1029/90JB02173.
- Nozaka, T., and P. Fryer (2011), Alteration of the oceanic lower crust at a slow-spreading axis: Insight from vein-related zoned halos in olivine gabbro from Atlantis Massif, Mid-Atlantic Ridge, *J. Petrol.*, 52(4), 643–664, doi:10.1093/ptrology/egq098.
- O'Hanley, D. (1992), Solution to the volume problem in serpentinization, *Geology*, 20(8), 705–708, doi:10.1130/0091-7613(1992)020<0705:STTVPI>2.3.CO;2.
- Ohara, Y., T. Yoshida, Y. Kato, and S. Kasuga (2001), Giant megamullion in the Parece Vela backarc basin, *Mar. Geophys. Res.*, 22(1), 47–61, doi:10.1023/A:1004818225642.
- Okino, K., K. Matsuda, D. Christie, Y. Nogi, and K. Koizumi (2004), Development of oceanic detachment and asymmetric spreading at the Australian-Antarctic Discordance, *Geochem. Geophys. Geosyst.*, 5, Q12012, doi:10.1029/2004GC000793.
- Olive, J., M. Behn, and B. Tuelholke (2010), The structure of oceanic core complexes controlled by the depth distribution of magma emplacement, *Nat. Geosci.*, 3(7), 491–495, doi:10.1038/NNGEO888.
- Penrose Conference Participants (1973), Penrose field conference: Ophiolites, *Geotimes*, 17, 24–26.
- Planert, L., E. Flueh, and T. Reston (2009), Along-and across-axis variations in crustal thickness and structure at the Mid-Atlantic Ridge at 5°S obtained from wide-angle seismic tomography: Implications for ridge segmentation, *J. Geophys. Res.*, 114, B09102, doi:10.1029/2008JB006103.
- Reston, T., et al. (2002), A rifted inside corner massif on the Mid-Atlantic Ridge at 5°S, *Earth Planet. Sci. Lett.*, 200(3–4), 255–269, doi:10.1016/S0012-821X(02)00636-2.
- Schroeder, T., and B. John (2004), Strain localization on an oceanic detachment fault system, Atlantis Massif, 30°N, Mid-Atlantic Ridge, *Geochem. Geophys. Geosyst.*, 5, Q11007, doi:10.1029/2004GC000728.
- Searle, R., M. Cannat, K. Fujioka, C. Mével, H. Fujimoto, A. Bralée, and L. Parson (2003), Fuji dome: A large detachment fault near 64°E on the very slow-spreading Southwest Indian Ridge, *Geochem. Geophys. Geosyst.*, 4(8), 9105, doi:10.1029/2003GC000519.
- Seher, T., W. Crawford, S. Singh, M. Cannat, V. Combier, and D. Dusunur (2010), Crustal velocity structure of the Lucky Strike segment of the Mid-Atlantic Ridge at 37°N from seismic refraction measurements, *J. Geophys. Res.*, 115, B03103, doi:10.1029/2009JB006650.
- Sempéré, J., et al. (1995), The Mid-Atlantic Ridge between 29°N and 31°30'N in the last 10 Ma, *Earth Planet. Sci. Lett.*, 130(1), 45–55, doi:10.1016/0012-821X(94)00259-2.
- Shtivelman, V., and A. Canning (1988), Datum correction by wave-equation extrapolation, *Geophysics*, 53(10), 1311–1322, doi:10.1190/?1.1442409.
- Smith, D., and J. Cann (1993), Building the crust at the Mid-Atlantic Ridge, *Nature*, 365(6448), 707–715, doi:10.1038/365707a0.
- Smith, D., J. Cann, and J. Escartín (2006), Widespread active detachment faulting and core complex formation near 13°N on the Mid-Atlantic Ridge, *Nat. Lett.*, 442, 440–443, doi:10.1038/nature04950.
- Smith, D., J. Escartín, H. Schouten, and J. Cann (2008), Fault rotation and core complex formation: Significant processes in seafloor formation at slow-spreading mid-ocean ridges (Mid-Atlantic Ridge, 13–15°N), *Geochem. Geophys. Geosyst.*, 9, Q03003, doi:10.1029/2007GC001699.
- Spudich, P., and J. Orcutt (1980), A new look at the seismic velocity structure of the oceanic crust, *Rev. Geophys.*, 18(3), 627–645, doi:10.1029/RG018i003p00627.
- Tolstoy, M., A. Harding, and J. Orcutt (1993), Crustal thickness on the Mid-Atlantic Ridge: Bull's-eye gravity anomalies and focused accretion, *Science*, 262(5134), 726–729, doi:10.1126/science.262.5134.726.
- Tuelholke, B., and J. Lin (1994), A geological model for the structure of ridge segments in slow spreading ocean crust, *J. Geophys. Res.*, 99(B6), 11,937–11,958, doi:10.1029/94JB00338.
- Tuelholke, B., J. Lin, and M. Kleinrock (1998), Megamullions and mullion structure defining oceanic metamorphic core complexes on the Mid-Atlantic Ridge, *J. Geophys. Res.*, 103(B5), 9857–9866, doi:10.1029/98JB00167.
- Tuelholke, B., K. Fujioka, T. Ishihara, G. Hirth, and M. Kinoshita (2001), Submersible study of an oceanic megamullion in the central north Atlantic, *J. Geophys. Res.*, 106(B8), 16,145–16,161, doi:10.1029/2001JB000373.
- Tuelholke, B., M. Behn, W. Buck, and J. Lin (2008), Role of melt supply in oceanic detachment faulting and formation of megamullions, *Geology*, 36(6), 455–458, doi:10.1130/G24639A.1.
- Van Avendonk, H., D. Shillington, W. Holbrook, and M. Hornbach (2004), Inferring crustal structure in the Aleutian Island Arc from a sparse wide-angle seismic data set, *Geochem. Geophys. Geosyst.*, 5, Q08008, doi:10.1029/2003GC000664.
- Wessel, P., and W. Smith (1991), Free software helps map and display data, *Eos Trans. AGU*, 72(441), 445–446.
- White, R., D. McKenzie, and R. O'Nions (1992), Oceanic crustal thickness from seismic measurements and rare earth element inversions, *J. Geophys. Res.*, 97(B13), 19,683–19,715, doi:10.1029/92JB01749.
- Xu, M., J. Canales, B. Tuelholke, and D. DuBois (2009), Heterogeneous seismic velocity structure of the upper



- lithosphere at Kane oceanic core complex, Mid-Atlantic Ridge, *Geochem. Geophys. Geosyst.*, *10*, Q10001, doi:10.1029/2009GC002586.
- Zelt, C., and P. Barton (1998), Three-dimensional seismic refraction tomography: A comparison of two methods applied to data from the Faeroe Basin, *J. Geophys. Res.*, *103*(84), 7187–7210, doi:10.1029/97JB03536.
- Zervas, C., J. Sempéré, and J. Lin (1995), Morphology and crustal structure of a small transform fault along the Mid-Atlantic Ridge: The Atlantis Fracture Zone, *Mar. Geophys. Res.*, *17*(3), 275–300, doi:10.1007/BF01203466.